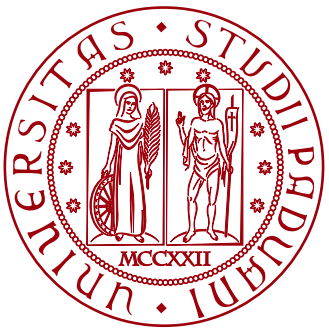

UNIVERSITÀ DEGLI STUDI DI PADOVA

Dipartimento di Fisica e Astronomia "Galileo Galilei"

Master Degree in Physics

Final Dissertation

Screening effects in Alkali-Halide nanostructures

Thesis supervisor
Prof. Pier Luigi Silvestrelli
Co-supervisor
Dr. Alberto Ambrosetti

Candidate
Matteo Tessarolo

Academic Year 2022/2023

Abstract

Nanostructures are interesting systems for the scientific research, both from a theoretical and an experimental point of view, also because they allow to investigate a wide range of phenomena. In particular, the recent discovery of a "chemical surgery" method to insert ions or small molecules inside buckminsterfullerene C_{60} increased further the interest about the endohedral nanostructures. When a polar molecule, like water, is encapsulated inside a fullerene the total electric dipole moment of the endohedral structure is the result of the interaction of the molecule with the surrounding nanostructure and, according to independent first-principles calculations, is significantly reduced with respect to that of an isolated water molecule ("screening" effect). The investigation has been subsequently extended to larger nanostrutures and nanocages composed of atoms different from carbons. By evaluating the dipole moment of endohedral nanocages, it was found that the screening effect crucially depends on the nature of the intramolecular bonds of the surrounding nanocage: in particular, it is maximized by covalent-bond carbon nanostructures, while interestingly, alkali-halide, fullerene-like nanocages, exhibit instead an "antiscreening" effect since they act as dipole-moment amplifiers. The aim of this thesis work is the first-principles characterization of the antiscreening effect in other nanostructures, namely alkali-halide nanotubes, this choice being motivated by recent theoretical and experimental studies concerning the stability and the many potential applications of these nanotubes. In particular, we have considered, as the most promising systems, nanotubes with octagonal transversal section and six layers in the longitudinal direction. As a preliminary step the stability of nanotubes made by different binary combinations of alkali metals and halides has been performed, finding that the Lithium-Fluoride (LiF) nanotube is the most stable one. Next we have investigated, by first-principles techniques based on the Density Functional Theory (DFT), the properties of endohedral alkali-halide nanotubes obtained by encapsulation of a water molecule, similarly to what done in previous applications to alkali-halide, fullerene-like nanocages. Basically, all the considered alkali-halide nanotubes, with octagonal transversal section, exhibit a characteristic antiscreening effect, which tends to increase as a function of the number of layers in the longitudinal direction. Interestingly, the specific geometric structure of the nanotube seems to be crucial for triggering the antiscreening phenomenon. In fact, calculations on an endohedral nanostructure with dodecagonal section (instead of octogonal) indicate a reduction of the total dipole moment, so that a screening behavior similar to that observed in more conventional carbon nanocages is observed. Finally, we have also studied endohedral $Li_{24}F_{24}$ nanostructures where the encapsulated water molecule is replaced by linear, ionic-bonded molecules, NaF and LiF having a dipole moment even larger that that of the water molecule.

Contents

Introduction

Nanostructures (in particular gaphene, fullerenes and carbon nanotubes) are gaining increasing interest in the field of research, both from a theoretical and an experimental point of view. Graphene, a single layer hexagonal lattice of carbon atoms, was discovered in 2004 by the group of Andre Geim and Konstantin Novoselov, and earned them the Nobel Prize in 2010. Graphene is an outstanding material due to its peculiar mechanical properties and its behaviour as gapless semiconductor [1], which make it quite promising for countless electronic, sensor, biomedical and material science applications. For instance, the GFET (Graphene Field Effect Transistor) is a potential supplement to silicon CMOS (Complementary Metal-Oxide Semiconductor) transistors, with extremely attractive performances [2]. As shown in Fig. 1 , a portion of a graphene layer can be bended to form a buckminsterfullerene (0D structure), a carbon nanotube (1D structure) or stacked into graphite (3D structure).

Due to its stability and abundance, C_{60} buckminsterfullerene has attracted great attention and interest since its discovery.[3]. Similarly to graphene, the buckyball nanostructure exhibits electrical, optical and chemical attractive properties. The interest about this nanostructure is further increased by the discovery of a "molecular surgery" tehcnique to encapsulate metal ions, noble gases or small molecules.[4] [5] [6] [7] [8] [9] This technique consists in a sequence of organic reactions aimed to create a stable hole in the buckyball, insert a specific molecule with adequate pressure and temperature, and close the hole. A nanostructure with a molecule encapsulated inside is called "endohedral" structure. The interaction between a polar molecule, such as HF, LiF or H_2O and the nanostructure encapsulating it, generates a displacement of the atoms and a distortion of the electron density. According to the DFT calculations of Kurotobi and Murata the endohedral complex $H_2O@C_{60}$ is characterized by a total dipole moment, comparable to the one of the isolated water molecule [8]. Subsequent, more accurate DFT calculations [10] [11] [12] have instead verified that the total dipole moment of $H_2O@C_{60}$ is significantly reduced (0.5 D) with respect to that (1.8 D) of isolated H_2O, thus clearly suggesting a significant screening effect due to the C_{60} nanocage. In Fig. 2 this phenomenon is illustrated by plotting the differential charge density induced by the incapsulation of a water molecule inside the C_{60} buckyball: red

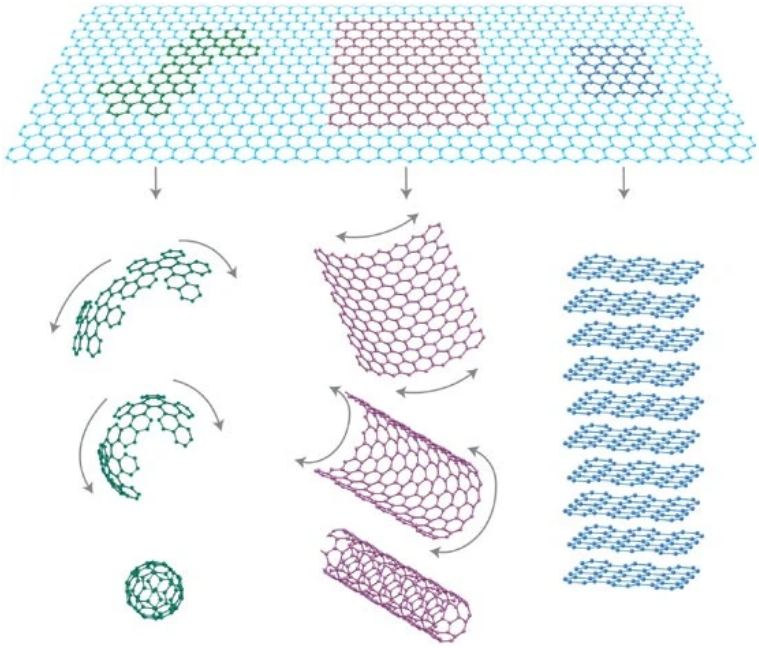

Fig. 1: Four allotropes of carbon

and blue volumes represent the electron density gain and loss, respectively [13].

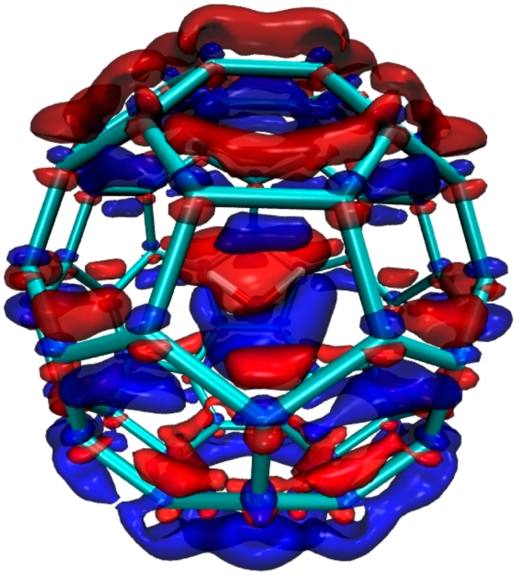

Fig. 2: Polarization of $H_2O@C_{60}$

Since the screening effect is certainly related to the distribution of the charge density of the valence electrons and therefore to the characteristic covalent nature of the carbon-carbon bonds in the buckyball, it is interesting to investigate what happens if nanocages characterized by a different kind of bonds, for instance ionic bonds, are considered. To this aim, the encapsulation of small polar molecules in alkali-halide nanocages has been simulated by first-principles in ref. [14], using the Quantum-ESPRESSO computational package[15]. These nanocages are designed to have a geometry similar to a fullerene, which is close to a spherical geometry, even

though they are unable to have pentagonal faces because of their binary composition. Interestingly, most of these alkali-halide nanocages, exhibit an "antiscreening" effect since the dipole moment of the endohedral complex is larger than that of the encapsulated polar molecule, by 30% to 70%, depending on the adopted nanocage. Only alkali-halide nanocages, characterized by a reduced ionic nature, such as $B_{36}N_{36}$ and $Be_{36}O_{36}$, are found to screen the dipole moment of the encapsulated molecule, similarly to what observed with carbon nanocages. In light of these results it is clearly interesting to extend the study to different nanostructures, such as the nanotubes. Alkali-halide nanotubes are currently investigated both experimentally and theoretically; in particular the research focused on LiF nanotubes and the possibility of obtaining experimentally these nanostructures by the impact of fast ions on a LiF polycrystal [13] [16] [17] [18]. The most stable nanotube structure turns out to be characterized by an octagonal base and six layers, which corresponds to 24 LiF pairs. When compared to the more traditional carbon (diameter from 10 to 20 Å), BN (10÷30 Å), or GaN (300÷2000 Å) nanotubes, these alkali-halide nanostructures are narrower, with a diameter between 2 and 7 Å. This is due to the fact that alkali-halide nanotubes, in contrast to those made of other compositions, show stable structures for very small cross-sections (hexagonal/octagonal). The reference system for this thesis work is the endohedral complex $H_2O@Li_{24}F_{24}$, namely a lithium fluoride octagonal nanotube made of six layers encapsulating a water molecule. First-principles calculations have been performed using the Quantum-ESPRESSO computational package, within the framework of the Density Functional Theory (DFT). Particular attention has been devoted to the London dispersion forces, that are purely quantum interactions which require appropriate formulations to be correctly evaluated in a DFT approach. In fact, although these interactions are much weaker than, for instance, those characterizing covalent or ionic bonds, nonetheless they are essential to obtain an accurate description of the interaction and binding energy between the encapsulated polar molecule and the surrounding nanocage. A detailed analysis has been performed to select computational parameters able to guarantee a good convergence in the basic structural, energetic an electronic properties of the investigated systems. The approach used to accurately describe the screening/antiscreening effect is similar to that adopted in ref. [14]. It basically consists in the evaluation of the dipole moment from the valence electron density distribution and the nuclei positions, in the analysis of the differential charge density, and in the calculation of the relative displacements of positive and negative ions of the alkali-halide nanotube upon encapsulation of a small molecule. The most relevant result is represented by the conclusion that antiscreening effects are also predicted in many alkali-halide nanotubes. For instance, the dipole moment of the endohedral complex $H_2O@Li_{24}F_{24}$ is significanly larger (by 31%) than that of the isolated water molecule, with a small but appreciable distortion of the $Li_{24}F_{24}$ nanotube. Extension of

the analysis to alkali-halide nanotubes composed of different elements or/and characterized by a different structure and different number of layers, and also to encapsulation of other polar molecules, such as LiF and NaF, qualitatively confirms the basic results previously obtained in the study of endohedral alkali-halide nanocages[14] but also elucidates the crucial role of the specific nanotube geometry.

Chapter 1

Methods

1.1 Density Functional Theory

The origin of the Density Functional Theory can be traced back to idea by Thomas and Fermi in 1927 to describe the electronic structure in terms of a local density of N electrons $\rho(\vec{r})$:

$$\int d\vec{r}\rho(\vec{r}) = N \tag{1.1}$$

According to this paradigm, the functional $E_{TF}[\rho]$, as shown in the Eq. 1.2, describes the energy associated to the density function $\rho(\vec{r})$ as sum of a kinetic component, a direct Hartree-like interaction energy between electrons given by $V(\vec{r}-\vec{r}')$, and a electron-nuclei interaction term given by $U(\vec{r})$.

$$E_{TF}[\rho] = \int d\vec{r}\frac{3}{5}\frac{\hbar^2}{2m}\left(3\pi^2\right)^{2/3}\rho\left(\vec{r}\right)^{5/3} + \frac{1}{2}\int d\vec{r}d\vec{r}'\rho(\vec{r})V(\vec{r}-\vec{r}')\rho(\vec{r}') + \int d\vec{r}U(\vec{r})\rho(\vec{r}) \tag{1.2}$$

It is possible to solve the variational problem of the energy functional minimization by introducing a suitable Lagrange multiplier ϵ. 1.3 is the equation that results from the minimization procedure:

$$\frac{\hbar^2}{2m}\left(3\pi^2\right)^{2/3}\rho\left(\vec{r}\right)^{2/3} + U(\vec{r}) + U_{mf}(\vec{r}) = \epsilon \tag{1.3}$$

The Eq. 1.4 defines the term $U_{mf}(\vec{r})$ as a Hartree-like mean-field potential acting on the electrons.

$$U_{mf}(\vec{r}) = \int d\vec{r}'V(\vec{r}-\vec{r}')\rho(\vec{r}') \tag{1.4}$$

This first formulation from Thomas and Fermi misses a fundamental component, the energy of exchange and correlation. In this respect Pierre Hohenberg and Walter Kohn provided an accurate theoretical reformulation of the DFT in 1964 [19], laying the groundwork for the modern DFT. In their work, Hohenberg and Kohn (HK) introduced formally a variational principle where the electron density function $\rho(\vec{r})$ is the variable function. This principle makes use of a universal function $F[\rho(\vec{r})]$, which applies to all electronic systems in their ground states no matter what the external potential is. The two HK theorems were first derived in relation to the investigation of non-degenerate ground states in the absence of a magnetic field, and they were subsequently generalised [20] [21].

The first HK theorem proves that the electron density function solely determines the ground state characteristics of a many-electron system. This makes it possible to reduce the computational problem to that of evaluating this basic quantity.

The second HK theorem, on the other hand, establishes an energy functional for the system and shows that the ground state's electron density minimises it.

Equation 1.5 indicates that the electron density used in the two HK theorems is practically evaluated from the orbitals $\phi_i(\vec{r})$ of the single electrons $i = 1 \dots N$.

$$\rho(\vec{r}) = \sum_{i=1}^{N} |\phi_i(\vec{r})|^2 \tag{1.5}$$

On the other hand, according to Eq. 1.6, the energy functional has two parts.

$$E[\rho] = F[\rho] + \int d\vec{r} U(\vec{r})\rho(\vec{r}) \tag{1.6}$$

The first component, $F[\rho]$, depends only on the electron-electron interaction, $V(\vec{r} - \vec{r}')$, because it is universal. Instead, the second component is entirely dependent on the external potential $U(\vec{r})$. The $F[\rho]$ functional is most commonly expressed using the formulation proposed by Walter Kohn and Lu Jeu Sham in 1965 [22]:

$$F_{KS}[\rho] = T_{KS}[\rho] + E_D[\rho] + E_{XC}[\rho] \tag{1.7}$$

The terms for kinetics ($T_{KS}[\rho]$), direct interaction ($E_D[\rho]$), and exchange-correlation ($E_{XC}[\rho]$) all occur in this formulation. The exchange-correlation term ($E_{XC}[\rho]$) is the most relevant and difficult of the three terms. The local Kohn-Sham equations for the orbitals $\phi_i(\vec{r})$ are obtained by minimizing the Kohn-Sham functional and normalising the density to N electrons, together with the usual Lagrange multiplier ϵ_i for each orbital. This variational technique produces a set of equations known as the Kohn-Sham equations, which have the form as in Eq. 1.8 for $i = 1 \dots N$.

$$\left[-\frac{\hbar^2}{2m}\nabla^2 + U(\vec{r}) + \int d\vec{r}' V(\vec{r}-\vec{r}')\rho(\vec{r}') + \frac{\delta E_{XC}[\rho]}{\delta\rho(\vec{r})}\right]\phi_i(\vec{r}) = \epsilon_i\phi_i(\vec{r}) \tag{1.8}$$

The theory formulated by Hohenberg, Kohn and Sham is the foundation of the present DFT. Recently, the practical implementation of the DFT has benefited from the introduction of new exchange-correlation functionals $E_{XC}[\rho]$ [23]. In particular, Nonlocal Correlations Functionals (NLCFs)[24], such as vdW-DF2 [25] and VV10[23], have gained popularity since they are more accurate and they contain less empirical parameters than other semiempirical functionals. Moreover, they allow a proper description of the Van der Waals interactions [26] [27], particularly the London dispersion forces, which arise from a purely quantum behaviour, since they consist in a forces between istantaneous induced dipoles. The VV10 energy functional expression is reported in Eq. 1.9, where $\Phi(\vec{r},\vec{r}')$ is the NLC kernel, $R = |\vec{r}-\vec{r}'|$.

$$\begin{aligned}
E_c^{VV10} &= \int d\vec{r}\rho(\vec{r})\left[\frac{1}{32}\left(\frac{3}{b^2}\right)^{3/4} + \frac{1}{2}\int d\vec{r}'\rho(\vec{r}')\Phi(\vec{r},\vec{r}')\right] \\
\Phi(\vec{r},\vec{r}') &= -\frac{3}{2}\left(gg'\left(g+g'\right)\right) \\
g &= \omega_0 R^2 + \kappa \\
\omega_0 &= \sqrt{C\left|\frac{\nabla\rho}{\rho}\right| + \frac{4\pi}{3}\rho} \\
\kappa &= \frac{3\pi b}{(576\pi)^{1/6}}\rho^{1/6}
\end{aligned} \tag{1.9}$$

This energy functional depends on two parameters; b controls the short range damping of r^{-6} while C controls the accuracy at the long range. The functions g, ω_0 and κ instead are intermediate steps to simplify the kernel definition, and the apex distinguishes which coordinates the function is calculated at ($g = g(\vec{r})$ and $g' = g(\vec{r}')$). The direct evaluation of the integral in the plane wave framework is computational demanding. The efficient implementation of NLCFs in plane-wave basis set codes has been made more affordable due to an interpolation scheme elaborated by Roman-Perez and Soler (RPS) [28]. By introducing an auxiliary variable $q(\vec{r}) = q(\rho(\vec{r}), |\nabla\rho(\vec{r})|)$, the NLCF kernel is expressed as in Eq. 1.10, where the interpolating functions P_i are defined so that $\sum_i P_i(q) = 1$ and $P_i(q_j) = \delta_{ij}$.

$$\Phi(q,q',R) \approx \sum_{ij} P_i(q(\vec{r}))\Phi(q_i,q_j,R)P_j(q(\vec{r}')) \tag{1.10}$$

Unfortunately the VV10 kernel depends separately on densities and gradient density in $\vec{r}$ and $\vec{r}'$, as reported in Eq. 1.11, and so a direct application of the RPS interpolation would be very computationally demanding.

$$\Phi^{VV10} = -\frac{3}{2}\kappa^{-3/2}\kappa'^{-3/2}\left(\frac{g}{\kappa}\frac{g'}{\kappa'}\left(\sqrt{\frac{\kappa}{\kappa'}}\frac{g}{\kappa} + \sqrt{\frac{\kappa'}{\kappa}}\frac{g'}{\kappa'}\right)\right)^{-1} \tag{1.11}$$

The last term containing the ratio $\sqrt{\frac{\kappa}{\kappa'}}$ depends directly on the density in both grid points $\vec{r}$ and $\vec{r}'$, and this prevents the VV10 kernel from being in a suitable form to be treated by the RPS procedure. To fix this inconvenient, Sabatini and coworkers performed several tests to investigate the behaviour of $\sqrt{\frac{\kappa}{\kappa'}}$ as function of R and ρ, as shown in Fig. 1.1. As result, it was determined that the ratio takes values in a narrow range around 1, and it is basically stable for R beyond 1 Å, with significant deviations only for points involving very low electron densities.

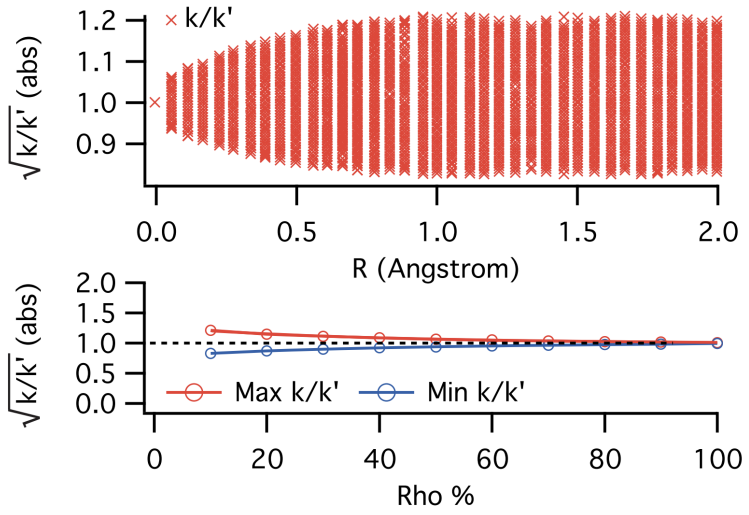

Fig. 1.1: $\sqrt{\frac{\kappa}{\kappa'}}$ as function of R and ρ

It can be concluded that the ratio can differ from the unity only when involving interacting charge far apart with each other and such that at least one is very small, and also in this case, it represents only a small contribution in the kernel since it is multiplied by the two charge densities. Hence it is natural to approximate $\sqrt{\frac{\kappa}{\kappa'}} \approx 1$ and so this term is dropped obtaining the Eq. 1.12 for the rVV10 kernel.

$$\Phi^{rVV10} = -\frac{3}{2}\kappa^{-3/2}\kappa'^{-3/2}\left(\frac{g}{\kappa}\frac{g'}{\kappa'}\left(\frac{g}{\kappa} + \frac{g'}{\kappa'}\right)\right)^{-1} \tag{1.12}$$

The original VV10 functional paired rPW86 [29] exchange and PBE [27] correlation and used as the optimized values for the empirical parameters: b=5.9 and C=0.0093. Sabatini and coworkers, retained the value of C, the basic exchange and correlation functional, but optimized the value of b=6.3, leading to the rVV10 scheme[30].

The external potential of a physical system made of N atomic nuclei, each with a charge Z_α, is expressed as a straightforward sum of Coulomb interactions between electrons and nuclei (see Eq. 1.13). It is convenient to exploit the Born-Oppenheimer approximation [31], which treats

atomic nuclei as classical, frozen objects and ignores their kinetic energy, to optimise the electron density distribution.

$$U\left(\vec{r}, \left\{\vec{R}_\alpha\right\}\right) = -\sum_{\alpha}^{N} \frac{Z_\alpha e^2}{4\pi\epsilon_0} \frac{1}{|\vec{R}_\alpha - \vec{r}|} \tag{1.13}$$

Then, using the Hellman-Feynman theorem, the forces acting on the nuclei can be determined, which allows a full structural relaxation of the system in its ground state, where the basic variables are the electron orbital functions $\phi_i(\vec{r})$ and the nuclei coordinates $\left\{\vec{R}_\alpha\right\}$.

1.2 Quantum-ESPRESSO

Quantum-ESPRESSO, a complete open-source suite for electronic and structural computations at the nanometric scale based on density functional theory, plane waves, and pseudopotentials, served as the primary tool for the realisation of this work. The basic computational program is **pw.x** (Plane-Wave Self-Consistent Field), which is an essential component of Quantum-ESPRESSO. The Kohn-Sham self-consistent equations are solved computationally by this software, as defined by Eq. 1.8. Starting from an initial electron density distribution, typically given by the sum of the densities of the isolated atoms, the code performs an iterative procedure to arrive at a self-consistent solution of the KS equations. In order to significantly reduce the (otherwise very demanding) computational effort, the interactions between nuclei and electrons are described using the so called "pseudopotentials" [32] [33] [34] which allow the practical simulation of only the valence electrons, while the core electrons are taken into account in an effective way. As already mentioned above, after optimising the electron density distribution, one can determine the forces on the nuclei and "relax" the structure of any system until the net forces acting on they nuclei are smaller than a given thresold. Bloch's theorem and crystal theory serve as the foundation for Quantum-ESPRESSO because it was developed specifically for the study of periodic systems where single-particle orbitals are expanded in a basis set of plane waves. The Bloch theorem [35] applies on systems subject to a periodic potential $U(\vec{r}) = U(\vec{r} + \vec{R})$, where $\vec{R} = m\vec{a} + n\vec{b} + l\vec{c}$ is a crystal vector. If the system evolves according to the Schrödinger equation with Hamiltonian $H = T + U$, the Bloch theorem states that the electron eigenstates have the form reported in Eq. 1.14, where n is the band index and $u_{n\vec{k}}(\vec{r})$ are the modulating functions with the same periodicity of the potential: $u_{n\vec{k}}(\vec{r}) = u_{n\vec{k}}(\vec{r} + \vec{R})$.

$$\psi_{n\vec{k}}(\vec{r}) = e^{i\vec{k}\cdot\vec{r}} u_{n\vec{k}}(\vec{r}) \tag{1.14}$$

Since the Bloch eigenstates $\psi_{n\vec{k}}(\vec{r})$ are associated to a specific wave vector $\vec{k}$, the total eigenfunction is obtained as a sum over all the wave vectors. This sum gives the KS orbitals, as reported in Eq. 1.15.

$$\phi_n(\vec{r}) = \sum_k \psi_{n\vec{k}}(\vec{r}) = \sum_k e^{i\vec{k}\cdot\vec{r}} u_{n\vec{k}}(\vec{r}) \tag{1.15}$$

In practice the sum is not performed over all the possible wave vectors, but only restricted to a finite set, determined by a kinetic energy cutoff (KEC), which only select the wave vectors (see Fig. 1.2) that satisfy the inequality $\frac{\hbar^2}{2m}|\vec{k} + \vec{G}|^2 \leq KEC$.

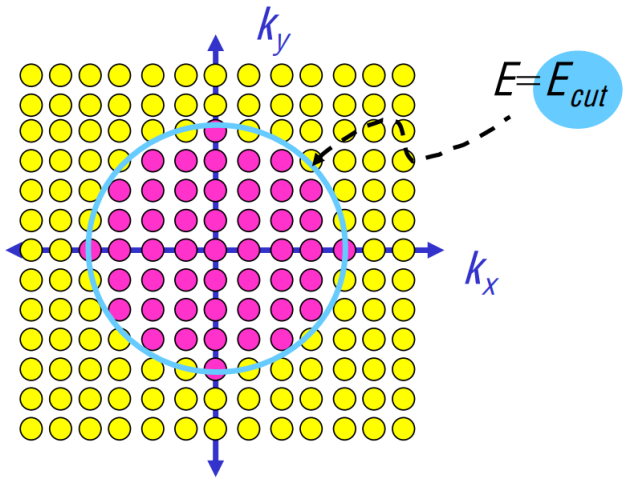

Fig. 1.2: Graphical representation of the kinetic energy cutoff in the wave-vector selection

The choice of the KEC parameter is crucial since a suitable compromise must be chosen between accuracy and computational effort. To this aim extended convergence tests have been carried out to determine the optimal KEC parameter (see the Results section).

Differential charge density analysis has been carried out by using the Quantum-ESPRESSO post-processing code **pp.x** which allows the generation of electron density maps (see Appendix for details).

1.3 Dipole evaluation

The electric dipole is defined as $\vec{p} = q\vec{d}$ in the case of a simple pair of opposite charges +q and -q separated by a vector distance $\vec{d}$, see Fig. 1.3.

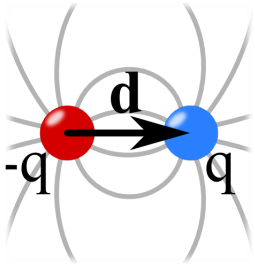

Fig. 1.3: Electric dipole moment

In a general system, characterized by a continous electron-charge distribution $\rho(\vec{r})$, the electronic dipole moment can be computed as reported by Eq. 1.16.

$$\vec{P}_{el} = -e \int d\vec{r}\vec{r}\rho(\vec{r}) \tag{1.16}$$

Then the total dipole moment is evaluated by taking into account also the distribution of the point-like ionic cores leading to the Eq. 1.17.

$$\vec{P} = -e \int d\vec{r}\vec{r}\rho(\vec{r}) + e\sum_{\alpha} Z_\alpha \vec{r}_\alpha \tag{1.17}$$

The electric dipole moment is expressed as $C{\cdot}m$ in SI units, however, for the study of electrical properties at the molecular level, a more convenient unit is the "Debye": $1D = 3.336{\cdot}10^{-30}\,Cm$. As an example, the dipole moment of an isolated H_2O molecule is near to 1.85 D [36]. Since the Quantum-ESPRESSO package does not explicitly compute the dipole moment, an additional program has been developed (by adopting the Python programming language) to evaluate $\vec{P}$ as in Eq. 1.17 by using as input data a three-dimensional array of the electron density distribution $\rho(\vec{r})$ and the optimized atomic coordinates. Note that Z_α refers to the number of valence electrons of atom α since the effect of the core electrons is taken into account by adopting the pseudopotential approach (see further details in table A.2).

Chapter 2

Results

2.1 Quantum-ESPRESSO settings

Before presenting the results, we briefly describe the basic technical parameters adopted for Quantum-ESPRESSO calculations (using the latest available 7.2 version). We used a simple tetragonal supercell simulation with periodic boundary conditions:

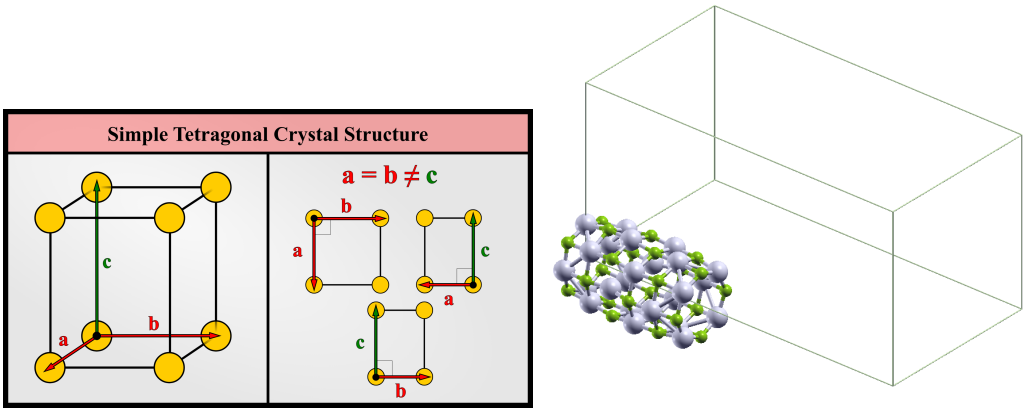

Fig. 2.1: Typical simulation model with a nanotube inside a simple tetragonal unit cell.

This lattice structure was chosen to optimize the ratio between the volume occupied by the structure and the total volume of the cell. Furthermore, the geometry denoted by $a = b \neq c$ allows the use of cells with dimensions rescaled homothetically with respect to the dimensions of the nanotube, with its axis along the z direction. In this way it is possible to obtain a uniform distance in all directions between periodic replicas of the nanostructure. In fact, as already mentioned, the object of the study is a single, isolated nanotube. The dimensions of the unit cell have been the subject of a detailed convergence study to find the best compromise between the computational effort and the accuracy of the results. The ratio of c, the dimension

along z, and a, the dimension along x and y, was kept constant and equal to 2, to match the typical dimensions of the nanotube. Extended convergence tests have been also carried out to find optimal values (in the range from 40 Ry to 100 Ry) for the KEC parameter (see Methods section) which determines the number of plane waves used to expand the single-particle orbitals. As mentioned above, the rVV10 DFT functional [26] [27], is particularly suited to describe inetracting systems where Van der Waals interactions can be important and, therefore, it has been used in the present calculations. Cohesive-energy estimates require the calculation of single-atom energies; hence, for atoms (such as Li and F) with an odd number of valence electrons, a spin polarized calculation is required, while this is not the case for the considered endohedral nanostructures that are all characterized by an even number of valence electrons. The energy-convergence threshold in the self consistent field calculations has been set to 10^{-8} Ry, two orders of magnitude smaller than the default value, in order to obtain highly accurate results. Finally, the sampling of the first Brillouin zone has been restricted to the center point, namely the Γ point, which is appropriate for the study of isolated nanostructures. Further technical details and the complete list of simulation parameters are reported in the appendix.

2.2 Energetic stability of alkali-halides nanostructures

We here analyze the stability of nanostructures with different chemical compositions but all characterized by the same geometrical structure: an octagonal nanotube of 6 layers, with 24 pairs of alkali-halide atoms, so 48 total atoms. In fact this structure turns out to be the most stable for the lithium fluoride composition and suitable for being experimentally realised [13]. 9 different chemical compositions have been considered, obtaining by combining alkali metals and halogen elements of periods 2, 3 and 4: LiF, LiCl, LiBr, NaF, NaCl, NaBr, KF, KCl and KBr. The basic parameter that determines the energy stability of the different nanotubes is represented by the cohesive energy per atom E_c, expressed by the relation 2.1, where E_{TOT} is the energy of the entire structure, made by N atoms, (obtained as the result of a full geometrical relaxation), while E_i are the energies of the isolated atoms (obtained by a simple Self-consistent field calculation).

$$E_c = \frac{1}{N}\left(\sum_i E_i - E_{TOT}\right) \tag{2.1}$$

For these calculations the dimensions of the adopted supercell are a=12 Å and c=24 Å, while the KEC parameter was set to 70 Ry. Table 2.1 reports the cohesive energies E_c of the selected nanotubes in eV/atom.

E_c [eV/at]	F	Cl	Br
Li	-4.226	-3.300	-2.878
Na	-3.649	-2.877	-2.572
K	-3.599	-2.931	-2.650

Table 2.1: Cohesive energy of alkali-halides nanotubes

In table 2.2 the computed cohesive energies are sorted in ascending order to obtain a ranking of the nanotubes from the most to the least stable.

Nanotube	E_c [eV/at]
$Li_{24}F_{24}$	-4.226
$Na_{24}F_{24}$	-3.649
K_{24} F_{24}	-3.599
$Li_{24}Cl_{24}$	-3.300
K_{24} Cl_{24}	-2.931
$Li_{24}Br_{24}$	-2.878
$Na_{24}Cl_{24}$	-2.877
K_{24} Br_{24}	-2.650
$Na_{24}Br_{24}$	-2.572

Table 2.2: Cohesive energies in ascending order of alkali-halides nanotubes

As said before, the cohesive energy of a nanostructure determines its stability. Although all

the considered nanotubes turn out to be stable, we decided to investigate in detail only the most stable ones, namely: $Li_{24}F_{24}$, $Na_{24}F_{24}$, $K_{24}F_{24}$, $Li_{24}Cl_{24}$, $K_{24}Cl_{24}$. In Fig. 2.2 the most stable nanotube is shown, that is $Li_{24}F_{24}$.

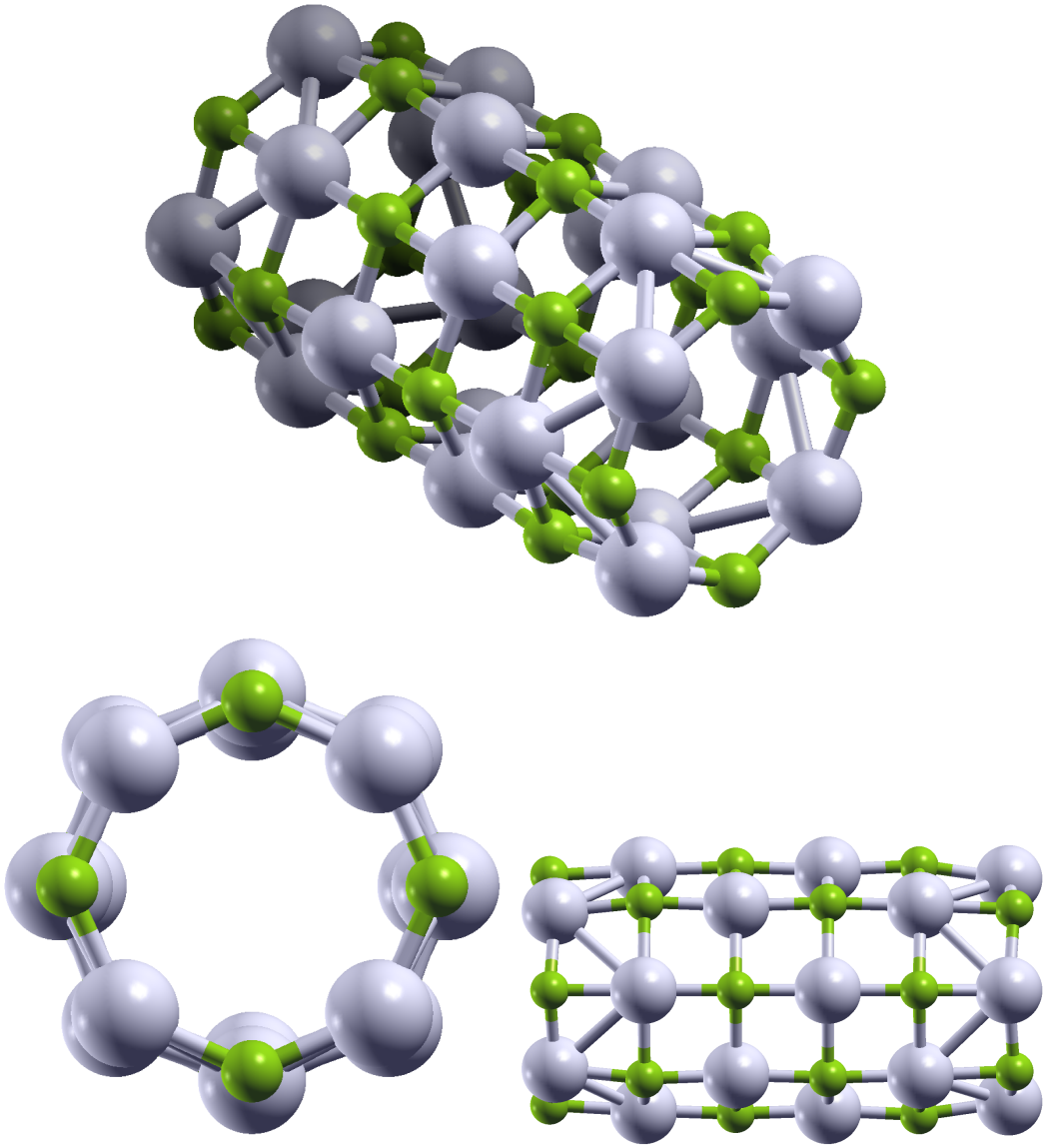

Fig. 2.2: $Li_{24}F_{24}$. Grey and green balls denote F and Li atoms, respectively.

2.3 Convergence study

In order to ensure the accuracy of the results obtained from first-principles DFT simulations a detailed convergence study was performed. The key parameters that have been varied are two, the unit cell size and the KEC value. In principle the largest possible values for these parameters should be chosen in order to get accurate results. In fact a large size of the simulation supercell allows to reduce spurious interactions between the periodic images of the nanostructure, thus approaching the description of a truly isolated structure. Moreover, a large value of the KEC parameter corresponds to a more complete expansion basis set. However, relatively large values of these parameters imply a considerable computational cost both in terms of occupied RAM memory and in terms of processing time, which respectively can exceed 16 GB and dozens of processing hours. It is therefore of considerable interest to determine the optimal parameters that guarantee stable results and an acceptable computational cost. The values chosen for the convergence study are the following:

- Size of the unitary cell : $a \in \{8, 9, 10, 11, 12, 13, 14, 15\}$ Å,$c = 2 \cdot a$
- kinetic energy cutoff : $E_{wfc} \in \{40, 50, 60, 70, 80, 90, 100\}$ Ry, wavefunction cutoff instead is six times the kinetic one.

The convergence study, carried out considering both isolated nanotubes and endhoedral nanostructures (with an encapsulated H_2O molecule) is performed in detail by evaluating the following features:

- Dimensional stability of the isolated $Li_{24}F_{24}$ nanotube;
- Cohesion energy of the isolated $Li_{24}F_{24}$ nanotube;
- Binding energy between $Li_{24}F_{24}$ nanotube and H_2O molecule;
- Stability of the position of the H_2O molecule along the axis of the nanotube;
- Orientation stability of the H_2O molecule in central position;
- Electric dipole moment of the isolated nanotube;
- Electric dipole moment of the isolated H_2O molecule;
- Total electric dipole moment of the endohedral complex $H_2O@Li_{24}F_{24}$;
- Distance between the centers of the positive Li+ and negative F- ions.

Dimensional stability of the isolated $Li_{24}F_{24}$ nanotube

In order to verify the adequate convergence of the structural optimization, we have monitored 4 distances characterizing the isolated $Li_{24}F_{24}$ nanotube (see Fig. 2.3):

- d_{AB} bond distance between two adjacent atoms of Lithium and Fluorine in the transversal direction at one end of the nanotube;
- d_{AC} bond distance between two adjacent atoms of Lithium and Fluorine in the longitudinal direction at one end of the nanotube;
- d_{DE} bond distance between two adjacent atoms of Lithium and Fluorine in the transverse direction at the center of the nanotube;
- d_{DF} bond distance between two adjacent atoms of Lithium and Fluorine in the longitudinal direction at the center of the nanotube.

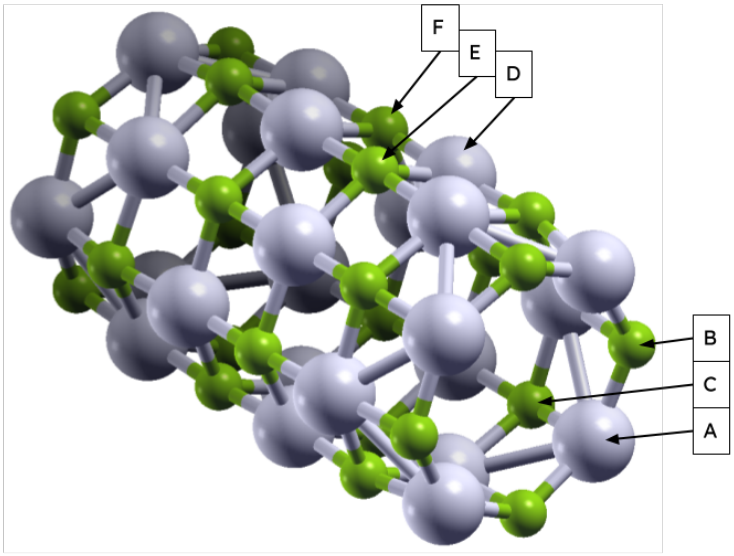

Fig. 2.3: Points used to define the four characteristic distances d_{AB},d_{AC},d_{DE} and d_{DF} of the $Li_{24}F_{24}$ nanotube

The results of the convergence analysis are reported in the tables 2.3 2.4 2.5 and 2.6. Fig. 2.4 shows the converging behaviour as a function of the unitary cell size and of the KEC parameter (the dotted lines are only a guide to the eyes). Sufficiently converged distances turn out to be: $d_{AB} = 1.78$Å, $d_{AC} = 1.86$Å, $d_{DE} = 1.91$Å and $d_{DF} = 1.87$Å. One can observe that the

transversal bond distance at the end of the nanotube d_{AB} is 7% smaller than the transversal bond distance at the center of the nanotube d_{DE}. The bond distance in the direction of the tube axis, on the other hand, does not show significant variations.

d_{AB} [Å]	**kinetic energy cutoff** [Ry]						
a [Å]	40	50	60	70	80	90	100
8	1.774	1.777	1.776	1.777	1.777	1.777	1.777
9	1.779	1.778	1.778	1.777	1.777	1.776	1.777
10	1.783	1.779	1.778	1.777	1.778	1.777	1.777
11	1.784	1.779	1.779	1.777	1.778	1.778	1.778
12	1.782	1.779	1.779	1.778	1.778	1.778	1.778
13	1.782	1.779	1.778	1.778	1.778	1.783	1.778
14	1.785	1.779	1.778	1.778	1.778	1.778	1.778
15	1.782	1.780	1.779	1.778	1.778	1.778	-

Table 2.3: Convergence of d_{AB} as a function of the unitary cell size and of the kinetic energy cutoff

d_{AC} [Å]	**kinetic energy cutoff** [Ry]						
a [Å]	40	50	60	70	80	90	100
8	1.850	1.853	1.853	1.853	1.853	1.853	1.853
9	1.856	1.855	1.855	1.855	1.854	1.854	1.854
10	1.853	1.856	1.857	1.857	1.856	1.855	1.855
11	1.849	1.857	1.858	1.857	1.856	1.857	1.855
12	1.852	1.857	1.858	1.858	1.856	1.856	1.856
13	1.853	1.857	1.860	1.858	1.857	1.857	1.856
14	1.852	1.857	1.859	1.856	1.857	1.857	1.857
15	1.855	1.857	1.857	1.858	1.856	1.855	-

Table 2.4: Convergence of d_{AC} as a function of the unitary cell size and of the kinetic energy cutoff

d_{DE} [Å]	**kinetic energy cutoff** [Ry]						
a [Å]	40	50	60	70	80	90	100
8	1.914	1.915	1.914	1.915	1.915	1.915	1.915
9	1.913	1.912	1.917	1.915	1.915	1.911	1.916
10	1.911	1.914	1.911	1.912	1.912	1.911	1.910
11	1.912	1.913	1.911	1.908	1.912	1.911	1.910
12	1.916	1.913	1.911	1.912	1.911	1.909	1.909
13	1.910	1.914	1.910	1.911	1.910	1.922	1.911
14	1.907	1.913	1.909	1.910	1.910	1.909	1.910
15	1.910	1.911	1.911	1.909	1.910	1.910	-

Table 2.5: Convergence of d_{DE} as a function of the unitary cell size and of the kinetic energy cutoff

d_{DF} [Å]		**kinetic energy cutoff** [Ry]						
		40	50	60	70	80	90	100
a [Å]	8	1.876	1.879	1.879	1.879	1.879	1.879	1.879
	9	1.888	1.885	1.883	1.884	1.885	1.883	1.885
	10	1.889	1.886	1.885	1.885	1.884	1.885	1.886
	11	1.884	1.883	1.887	1.888	1.885	1.885	1.885
	12	1.884	1.887	1.885	1.886	1.886	1.887	1.887
	13	1.895	1.887	1.887	1.887	1.885	1.884	1.884
	14	1.884	1.888	1.888	1.884	1.887	1.886	1.886
	15	1.891	1.887	1.885	1.884	1.886	1.886	-

Table 2.6: Convergence of d_{DF} as a function of the unitary cell size and of the kinetic energy cutoff

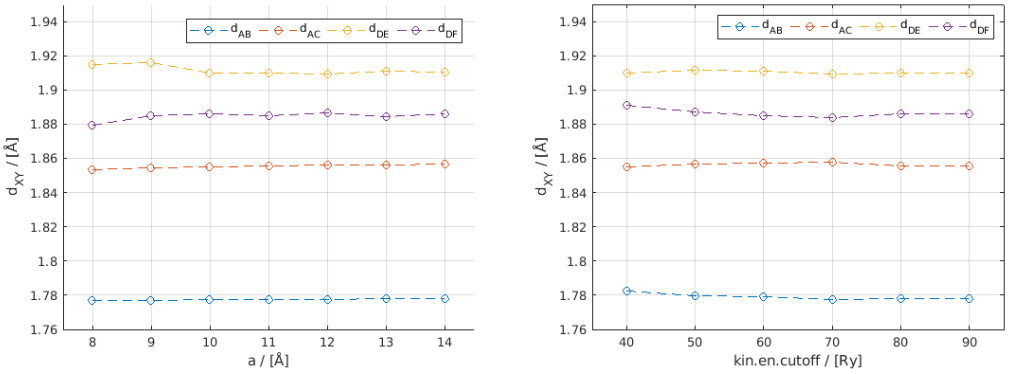

Fig. 2.4: Nanotube dimensions converging behaviour as a function of the unitary cell size and of the kinetic energy cutoff

Cohesive energy of the isolated $Li_{24}F_{24}$ nanotube

The behavior of the cohesive energy as a function of the unitary cell size and of the KEC parameter is reported in table 2.7 and shown in Fig. 2.5.

E_C [eV/at]		**kinetic energy cutoff** [Ry]						
		40	50	60	70	80	90	100
a [Å]	8	-4.165	-4.181	-4.184	-4.187	-4.188	-4.188	-4.188
	9	-4.193	-4.209	-4.212	-4.215	-4.216	-4.217	-4.210
	10	-4.203	-4.218	-4.221	-4.224	-4.226	-4.226	-4.216
	11	-4.205	-4.221	-4.225	-4.227	-4.228	-4.229	-4.217
	12	-4.206	-4.221	-4.225	-4.228	-4.228	-4.230	-4.217
	13	-4.205	-4.221	-4.225	-4.227	-4.227	-4.230	-4.217
	14	-4.203	-4.220	-4.225	-4.227	-4.226	-4.230	-4.218
	15	-4.202	-4.220	-4.225	-4.226	-4.225	-4.229	-

Table 2.7: Cohesive energy convergence as a function of the unitary cell size and of the kinetic energy cutoff

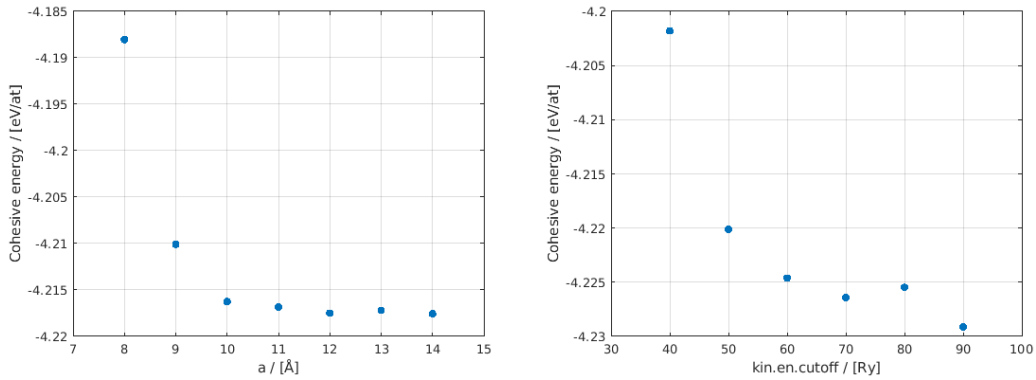

Fig. 2.5: Cohesive energy converging behaviour as a function of the unitary cell size and of the kinetic energy cutoff

A sufficiently converged value for the cohesive energy is about -4.2 eV/at. From the plots in Fig. 2.5 it can be seen that the cohesive energy fluctuations are suppressed for unitary cell sizes greater than a=12 Å and kinetic energy cutoff greater than 70 Ry. Therefore these values can be safely chosen as suitable parameters for accurate first-principles simulations. The converged size of the unit cell is a little smaller than 3 times the diameter of the nanotube, that is about 4.6 Å. Along the z axis, parallel to the axis of the nanotube, the dimension of the selected cell is 24 Å, against the 9.4 Å of the longitudinal dimension of the nanotube. The volume occupied by the nanotube is therefore approximately equal to 6% of the unitary cell value.

Binding energy between the $Li_{24}F_{24}$ nanotube and a water molecule

The binding energy between the nanotube and an encapsulated water molecule is defined as $E_B = E(H_2O@Li_{24}F_{24}) - E(Li_{24}F_{24}) - E(H_2O)$, where $E_B = E(H_2O@Li_{24}F_{24})$ is the total energy of the endohedral complex, $E(Li_{24}F_{24})$ the total energy of the $Li_{24}F_{24}$ nanotube, and $E(H_2O)$ that of the isolated water molecule. Clearly a negative value of the binding energy indicates that the water molecule energetically prefers to be encapsulated inside the nanotube rather than being isolated, although a significant energy barrier has to be probably overcome to penetrate the nanotube (see below). The converging behaviour of the binding energy as a function of the unitary cell size and the KEC parameter is reported in table 2.8 and in Fig. 2.6.

E_B [meV]		**kinetic energy cutoff** [Ry]						
		40	50	60	70	80	90	100
a [Å]	8	-283.4	-292.6	-292.2	-294.9	-295.2	-295.0	-294.5
	9	-232.3	-238.3	-238.2	-240.9	-242.2	-240.3	-241.7
	10	-218.4	-229.3	-226.0	-228.5	-227.8	-227.7	-227.0
	11	-225.7	-222.7	-223.3	-224.2	-225.7	-223.4	-224.1
	12	-217.6	-224.7	-223.2	-226.5	-224.4	-224.5	-224.2
	13	-218.4	-227.3	-225.2	-228.1	-224.3	-234.0	-224.6
	14	-216.1	-225.7	-224.4	-225.7	-225.1	-224.6	-225.0
	15	-219.4	-224.4	-224.2	-224.9	-224.8	-224.8	-

Table 2.8: Binding energy between $Li_{24}F_{24}$ and H_2O as a function of the unitary cell size and of the kinetic energy cutoff

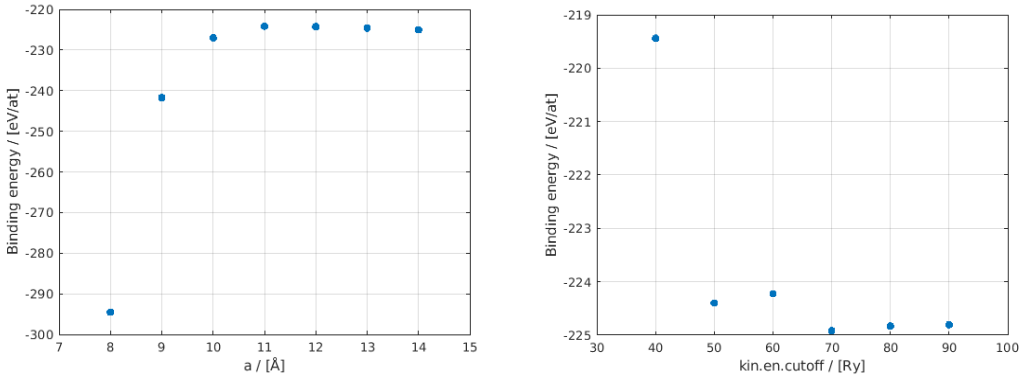

Fig. 2.6: Binding energy between $Li_{24}F_{24}$ and H_2O as a function of the unitary cell size and of the kinetic energy cutoff

A sufficiently converged value of the binding energy is $E_B = -225$ meV (so the endohedral structure is stable), with the fluctuations of this quantity that are certainly suppressed for unitary cell sizes greater than 12 Å and for a KEC value larger than 70 Ry, in line with what found in the study of the convergence behavior relative to isolated-nanotube features. It is interesting to evaluate also the stability of of the endohedral structure by changing the position of the molecule inside the nanotube, since the above converged value of the binding energy was computed by

placing the water molecule in the central position, with its dipole moment oriented parallel to the axis of the nanotube. Fig. 2.7 shows a longitudinal section of the nanotube which illustrates the central position of the water molecule.

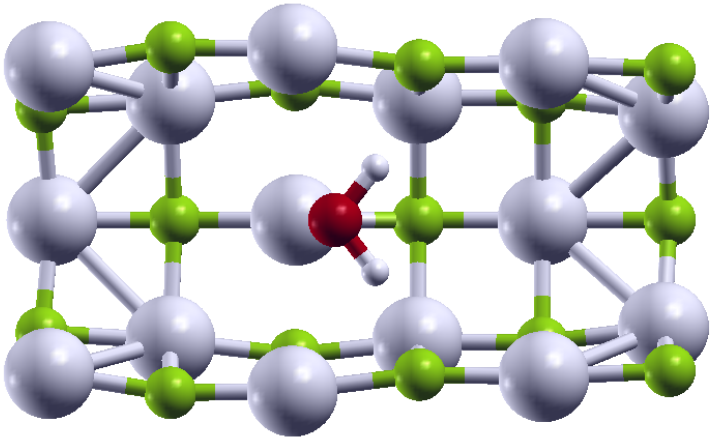

Fig. 2.7: Longitudinal section of the endohedral $H_2O@Li_{24}F_{24}$ complex showing the stable central position of the water molecule.

The stability analysis, reported in the next sections, has been performed by changing both the position and the orientation of the water molecule inside the nanotube. In particular, first the starting position of the molecule has been varied along the z axis of the nanotube but maintaining the same orientation and relaxing the structure; then only the orientation of the molecule, located in the center of the nanotube, has been varied. To reduce the computational cost of the many simulations required, this geometrical analysis has been carried out by adopting a slightly lower value of the KEC parameter (50 Ry) than that used for the other simulations (70 Ry).

Stability of the H_2O molecule along the nanotube axis

This section deals with the study of the stability of the H_2O molecule along the axis of the nanotube. This analysis was carried out by preparing a set of simulations in which the molecule, at the beginning of the structural optimization, is located in different positions along the axis, maintaining the orientation parallel to the nanotube axis as shown in Fig. 2.7. The chosen positions are uniformly arranged along the axis of the nanotube, from a few Å outside the nanotube to a few Å outside the opposite end. Fig. 2.8 reports two plots: on the left the final position of the molecule as a function of the initial one, in terms of the position along the z axis of the center of mass of the water molecule; on the right the dependence of the binding energy on the final position obtained from the structural optimization (the dashed line is only a guide to the eyes).

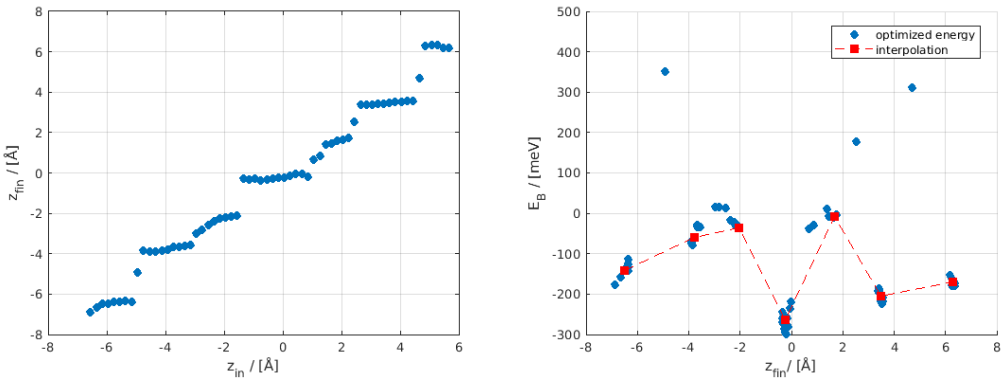

Fig. 2.8: Comparison between the initial and final positions in the structural optimization of the water molecule (left) and binding energy as a function of the optimized coordinate (right)

As can be seen in Fig. 2.9 several, different equilibrium positions of the water molecule inside the nanotube can be observed, corresponding to local minima.

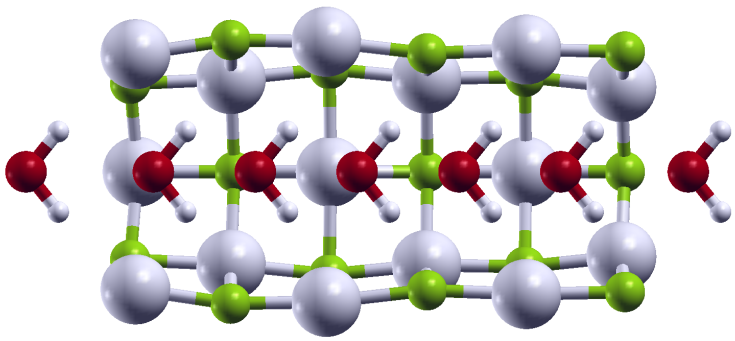

Fig. 2.9: Equilibrium position of the water inside the $Li_{24}F_{24}$ nanotube

Detailed analysis shows that these equilibrium positions are intermediate between the layers of the nanotube, so that the distance between the water molecule and the nanostructure atoms

is maximized. Interesting information can be also obtained from the graph showing the total energy behaviour as a function of the final positions of the structural optimization. As can be seen, the central position is confirmed to be the most stable one, while instead the two adjacent locations are much less energetically stable (-36 meV and -7 meV binding energies). Interestingly the first and last equilibrium positions are actually located outside the nanotube. The energy profile reported in Fig. 2.8 can give a rough estimate of the energy-barrier (activation energy) characterizing the encapsulation of the water molecule inside the nanotube, but in order to obtain a more accurate evaluation, a more sophisticated approach has been used, namely the Nudged Elastic Band (NEB) method combined with the climbing-image approach and the quasi-Newton Broyden's second method as the optimization scheme to investigate the full reaction path of the water molecule from outside to inside the nanotube [37] and to accurately determine the relative activation energy. The binding energies associated to the intermediate points of this path are plotted in Fig. 2.10. As can be seen, two main energy barriers are evident in the reaction path; the first (and the highest) one slightly outside the nanotube, with an energy barrier of 584 meV and the second, instead inside the nanotube, with an energy barrier of 320 meV. We can therefore conclude that encapsulation of H_2O inside $Li_{24}F_{24}$ requires overcoming an energy barrier of about 0.6 eV.

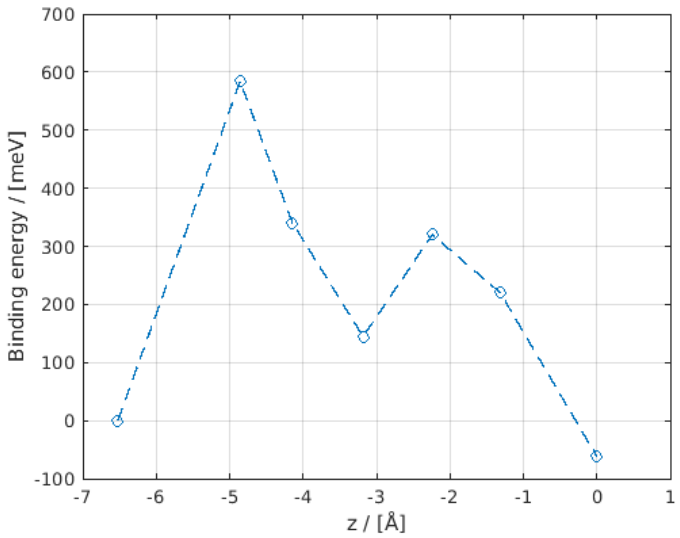

Fig. 2.10: NEB calculation for the water molecule reaction path inside the $Li_{24}F_{24}$ nanotube: binding energy as a function of the z coordinate of the O atom of the molecule

Stability of the H_2O orientation

In order to ensure that the initially chosen orientation, i.e. that characterized by an electric dipole moment parallel to the nanotube axis, is indeed the most stable one, a set of structural optimizations have been prepared where the H_2O molecule has an initial position with different directions. These orientations are defined by the angle θ shown in Fig. 2.11, i.e. the angle between the direction of the dipole moment of the water molecule and the z direction, which is coincident with the nanotube axis.

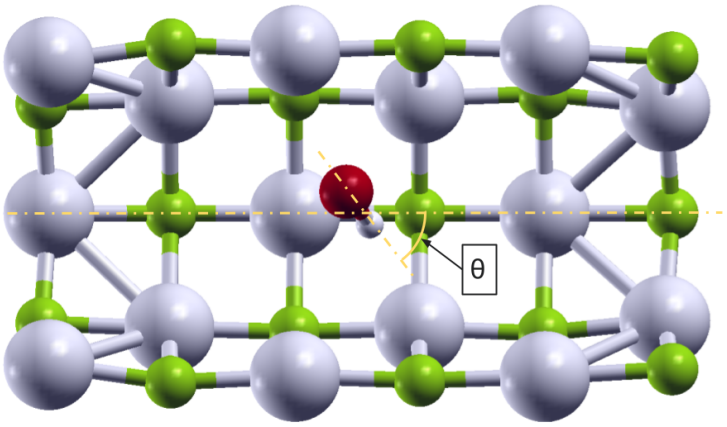

Fig. 2.11: Angle formed by the axis of the water molecule with the axis of the nanotube in the study of orientation stability

The orientations were choosen considering a uniform sampling within the $0° \div 90°$ range. In these simulations the center of mass of the water molecule was kept coincident with the center of the nanotube. The results of the structural optimizations were then analyzed by determining the final, optimized orientation of the molecule (see Fig. 2.12).

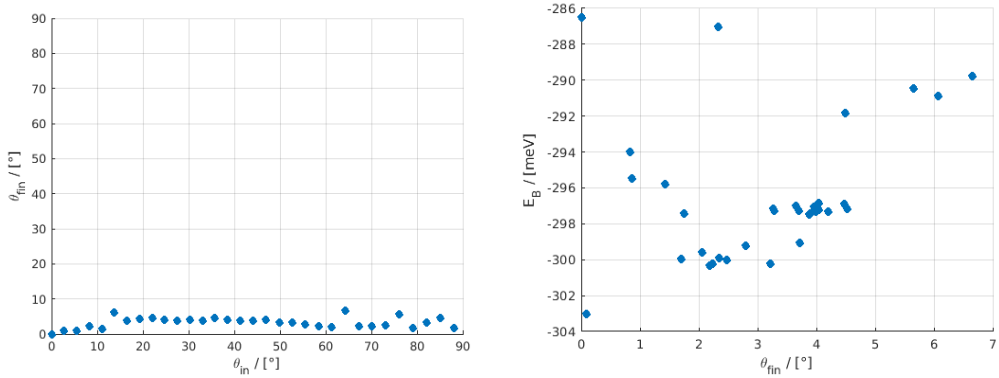

Fig. 2.12: Final orientations of the water molecule as a function of the initial orientations (left) and binding energies corresponding to the optimized angles (right)

As can be seen from the graph on the left, which shows the trend of the final angle of the water molecule as a function of the initial angle, the structural optimization brings the molecule back to form an angle with the z axis in most cases less than 5°. Moreover, considering the

behavior of the binding energy as a fucntion of the optimized angle (right panel), leads to the conclusion that the most stable orientation of the water molecule is indeed parallel to z, and so to the nanotube axis.

Dipole moment of the isolated $Li_{24}F_{24}$ nanotube

Table 2.9 reports the values of the electric dipole moment of the isolated $Li_{24}F_{24}$ nanotube. As expected on the basis of symmetry notions, this nanostructure turns out to be essentially apolar; in fact the value of the dipole moment tends to converge to zero as a function of the unitary cell size and the KEC parameter (see table 2.9 and Fig. 2.13). Once again the choice of 12 Å and 70 Ry as suitable parameters for convergence is confirmed.

μ_{isol} [D]		**kinetic energy cutoff** [Ry]						
		40	50	60	70	80	90	100
a [Å]	8	1.427	1.515	1.469	1.466	1.434	1.402	1.402
	9	0.671	0.410	0.606	0.557	0.544	0.326	0.535
	10	0.066	0.097	0.098	0.085	0.074	0.125	0.119
	11	0.118	0.052	0.069	0.008	0.025	0.016	0.048
	12	0.306	0.007	0.038	0.069	0.047	0.022	0.027
	13	0.305	0.111	0.099	0.085	0.041	0.230	0.054
	14	0.093	0.076	0.084	0.038	0.073	0.042	0.066
	15	0.187	0.061	0.086	0.035	0.067	0.058	-

Table 2.9: Electric dipole moment of isolated $Li_{24}F_{24}$ nanotube

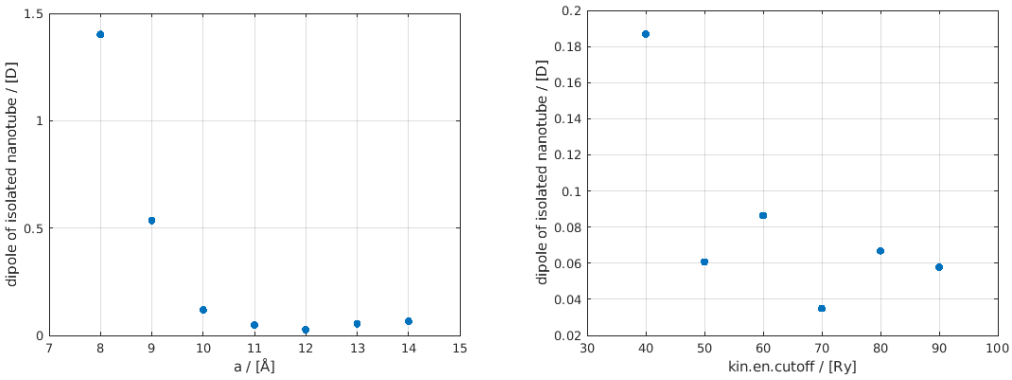

Fig. 2.13: Dipole of the isolated nanotube $Li_{24}F_{24}$ as a function of the unitary cell size and of the kinetic energy cutoff

Dipole moment of isolated water molecule

The values of the electric dipole moment of the water molecule are reported in table 2.10 and shown in Fig. 2.7 as a function of the unitary cell size and of the kinetic energy cutoff. As can be seen the dipole moment seems to reasonably converge to a value close to 1.8 D, which is compatible with the experimental reference estimate [36]. This provides a further confirmation of the correct determination of the electric dipole moment using the technique discussed above, i.e. by calculating the dipole from the electron density distribution and the positions of the atomic nuclei.

μ_{H_2O} [D]		**kinetic energy cutoff** [Ry]						
		40	50	60	70	80	90	100
a [Å]	8	1.7869	1.7869	1.7864	1.7867	1.7868	1.7866	1.7862
	9	1.7920	1.7920	1.7918	1.7918	1.7916	1.7919	1.7918
	10	1.7952	1.7951	1.7948	1.7950	1.7947	1.7949	1.7947
	11	1.7972	1.7976	1.7972	1.7972	1.7972	1.7968	1.7971
	12	1.7988	1.7991	1.7985	1.7982	1.7982	1.7985	1.7983
	13	1.7997	1.7996	1.7997	1.7997	1.7997	1.7995	1.7992
	14	1.8010	1.8007	1.8004	1.8003	1.8001	1.8004	1.8004
	15	1.8011	1.8012	1.8009	1.8012	1.8006	1.8007	-

Table 2.10: Electric dipole moment of isolated H_2O molecule

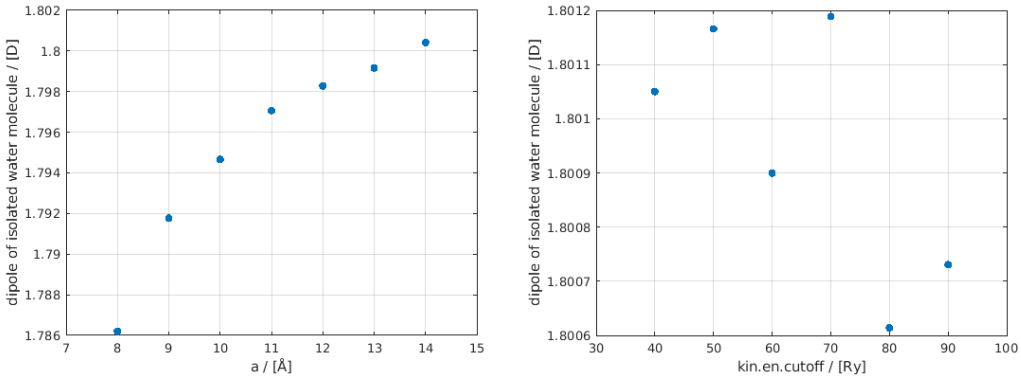

Fig. 2.14: Dipole of the isolated water molecule as a function of the unitary cell size and of the kinetic energy cutoff

Dipole moment of the $H_2O@Li_{24}F_{24}$ endohedral complex

The electric dipole moment of the $H_2O@Li_{24}F_{24}$ endohedral complex represents clearly the most relevant quantity to assess the screening/antiscreening character of the nanostructure. Its value as a function of the unitary cell size and of the kinetic energy cutoff is reported in table 2.11, and plotted in Fig. 2.15. As can be seen a well converged estimate (about 2.4 D) is obtained by adopting the usual size of the unit cell (12 Å) and the usual KEC parameter (70 Ry).

μ_{tot} [D]		**kinetic energy cutoff** [Ry]						
		40	50	60	70	80	90	100
a [Å]	8	3.59	3.44	3.41	3.38	3.37	3.37	3.36
	9	2.94	2.83	2.80	2.77	2.92	2.91	2.93
	10	2.44	2.40	2.40	2.49	2.39	2.49	2.50
	11	2.63	2.31	2.39	2.30	2.37	2.30	2.37
	12	2.87	2.25	2.31	2.47	2.31	2.39	2.39
	13	2.43	2.41	2.39	2.49	2.40	2.39	2.40
	14	2.43	2.34	2.42	2.41	2.41	2.41	2.41
	15	2.39	2.34	2.43	2.42	2.43	2.43	-

Table 2.11: Electric dipole moment of the $H_2O@Li_{24}F_{24}$ endohedral complex

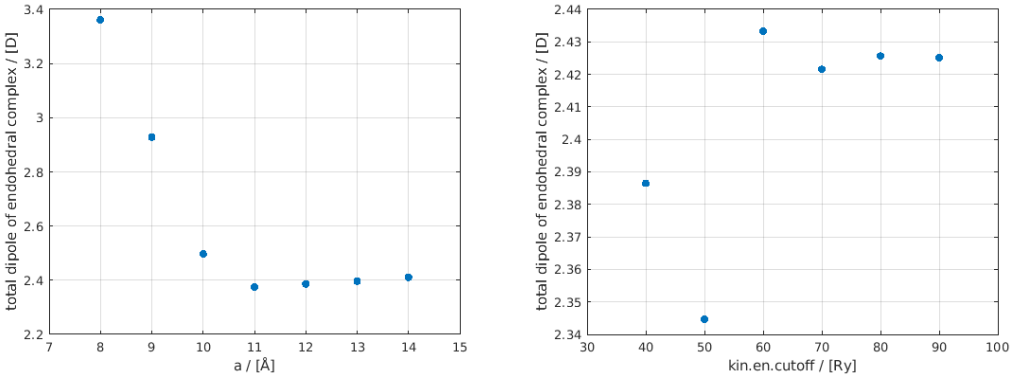

Fig. 2.15: Dipole of the $H_2O@Li_{24}F_{24}$ endohedral complex as a function of the unitary cell size and of the kinetic energy cutoff

Induced dipole moment

The induced dipole moment can be defined as the difference between the total dipole moment of the endohedral complex $H_2O@Li_{24}F_{24}$, the dipole of the isolated nanotube $Li_{24}F_{24}$ and that of the isolated water molecule: $\mu_{ind} = \mu_{tot} - \mu_{Li_{24}F_{24}} - \mu_{H_2O}$. Its value is reported in table 2.12 and plotted in Fig. 2.16 as a function of the unitary cell size and of the KEC parameter. The induced dipole moment is positive, with a converged value of 0.56 D, thus clearly indicating an antiscreening effect.

μ_{IND} [D]		**kinetic energy cutoff** [Ry]						
		40	50	60	70	80	90	100
a [Å]	8	0.375	0.141	0.154	0.126	0.152	0.178	0.173
	9	0.481	0.627	0.398	0.426	0.585	0.796	0.601
	10	0.576	0.511	0.507	0.609	0.523	0.572	0.584
	11	0.714	0.459	0.523	0.496	0.551	0.489	0.529
	12	0.762	0.446	0.476	0.603	0.461	0.566	0.561
	13	0.330	0.499	0.491	0.605	0.558	0.365	0.543
	14	0.540	0.459	0.533	0.573	0.541	0.572	0.545
	15	0.398	0.483	0.546	0.585	0.558	0.567	-

Table 2.12: Induced dipole moment

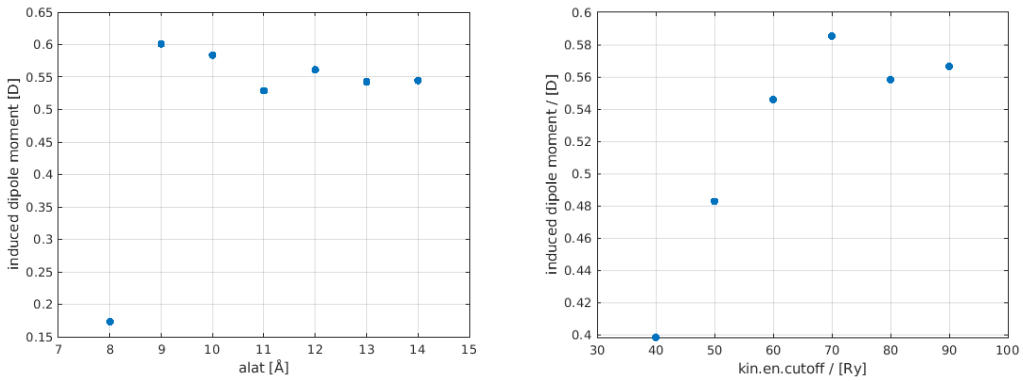

Fig. 2.16: Induced dipole moment as a function of the unitary cell size and of the kinetic energy cutoff

It is interesting to quantify this antiscreening effect in terms of a percentage variation of the total dipole with respect to that of the isolated H_2O molecule, according to the relation 2.2:

$$\Delta\mu_{\%} = \frac{\mu_{ind}}{\mu_{H_2O}} \cdot 100\% \tag{2.2}$$

The percent amplification of the dipole moment is reported in table 2.13 and plotted in Fig. 2.17 as a function of the unitary cell size and of the kinetic energy cutoff. From these data one can conclude that the converged percentage amplification is around a value of +31%.

$\Delta\mu_{\%}$ [%]		kinetic energy cutoff [Ry]						
		40	50	60	70	80	90	100
a [Å]	8	21.0	7.9	8.6	7.0	8.5	10.0	9.7
	9	26.8	35.0	22.2	23.8	32.6	44.4	33.5
	10	32.1	28.5	28.2	33.9	29.1	31.9	32.5
	11	39.7	25.6	29.1	27.6	30.7	27.2	29.4
	12	42.3	24.8	26.5	33.5	25.7	31.5	31.2
	13	18.4	27.7	27.3	33.6	31.0	20.3	30.2
	14	30.0	25.5	29.6	31.8	30.0	31.8	30.2
	15	22.1	26.8	30.3	32.5	31.0	31.5	-

Table 2.13: Percent amplification of the dipole moment of the $H_2O@Li_{24}F_{24}$ endohedral complex with respect to that of the isolated H_2O molecule.

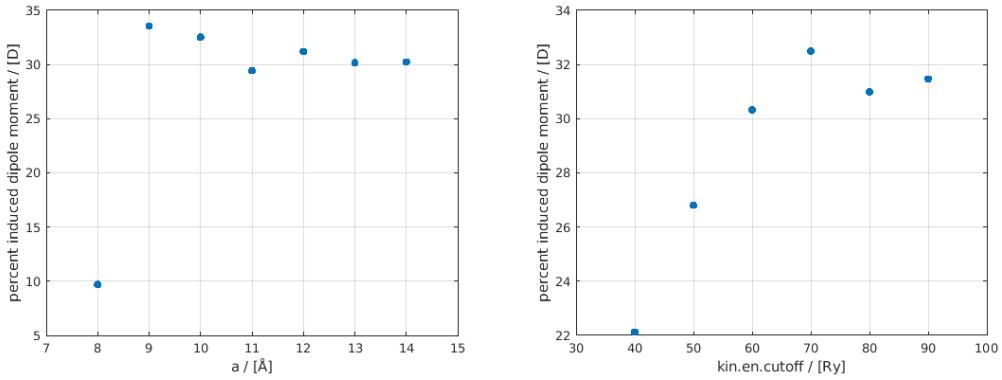

Fig. 2.17: Induced dipole moment as a function of the unitary cell size and of the kinetic energy cutoff

In order to better characterize this peculiar antiscreening effect with dipole amplification, further investigation is worthwhile. In particular, a useful quantity is represented by the differential charge density, defined as $\Delta\rho(\vec{r}) = \rho_{tot}(\vec{r}) - \rho_{isol}(\vec{r}) - \ \rho_{H_2O}(\vec{r})$, where $\rho_{tot}(\vec{r})$ is the charge density distribution of the $H_2O@Li_{24}F_{24}$ endohedral complex, after structural optimization. $\rho_{isol}(\vec{r})$ instead is the charge density of the isolated nanotube $Li_{24}F_{24}$ (assuming the atomic coordinates of the endohedral complex) and $\rho_{H_2O}(\vec{r})$, is the charge density of the isolated water molecule (again assuming the atomic coordinates of the molecule as inside the endohedral complex). In Fig. 2.18 and 2.19 we plot the differential charge density $\Delta\rho(\vec{r})$, looking at two selected planes: the first coincident with that of the water molecule and the second orthogonal to it. These pictures were obtained using the XCrySDen software [38], plotting isosurfaces corresponding to values of $\pm 5 \cdot 10^{-3} e/\text{Å}^3$: The red (blue) surface denotes electron density gain (loss) regions. As can be seen, the regions where the differential charge density is mostly localized are in the center of the nanotube, around the oxygen atom of the water molecule, and also in close vicinity of the two hydrogen atoms (in white) which face two lithium atoms (in green) of the nanotube.

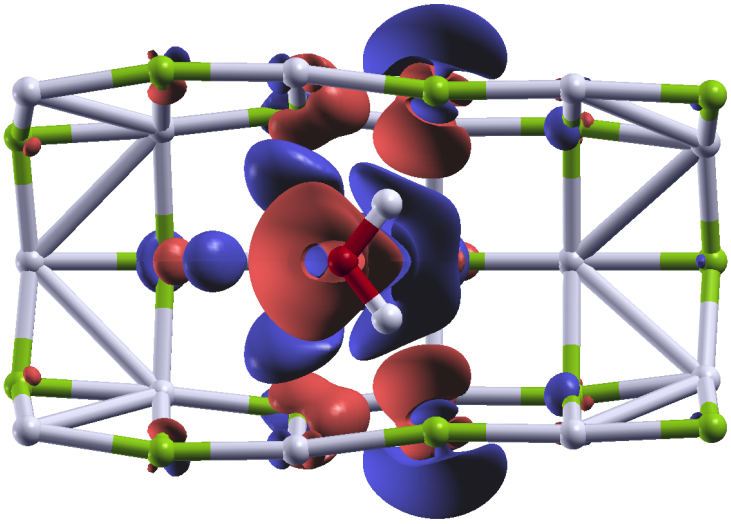

Fig. 2.18: Differential charge density plotted on a section coincident with the water molecule plane

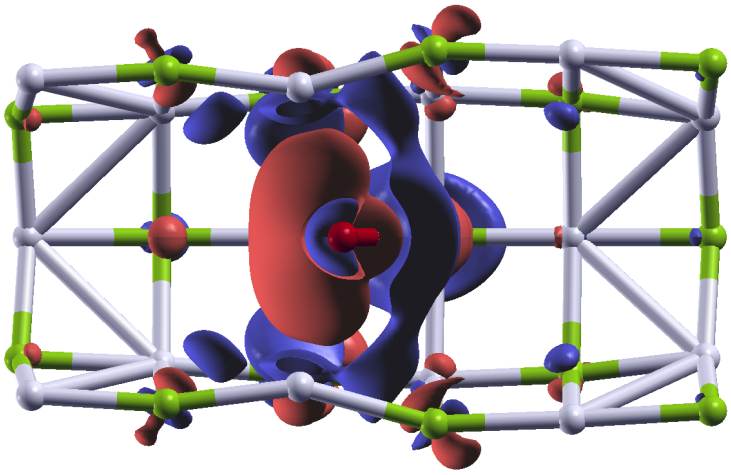

Fig. 2.19: Differential charge density plotted on a section orthogonal to the water molecule plane

Further information can be achieved by considering the one-dimensional profile of the differential electron density $\Delta\rho(z)$, computed along the z axis of the nanotube axis, by integrating $\Delta\rho$ defined above over the corresponding, orthogonal x, y planes. $\Delta\rho_+(z)$ is instead defined as above, but restricted only to positive values of $\Delta\rho$, while $\Delta\rho_-(z)$ is restricted only to negative values. The plots of these functions are shown in Fig. 2.20, where the black, dotted lines define the physical boundaries of the nanotube considering the z coordinate.

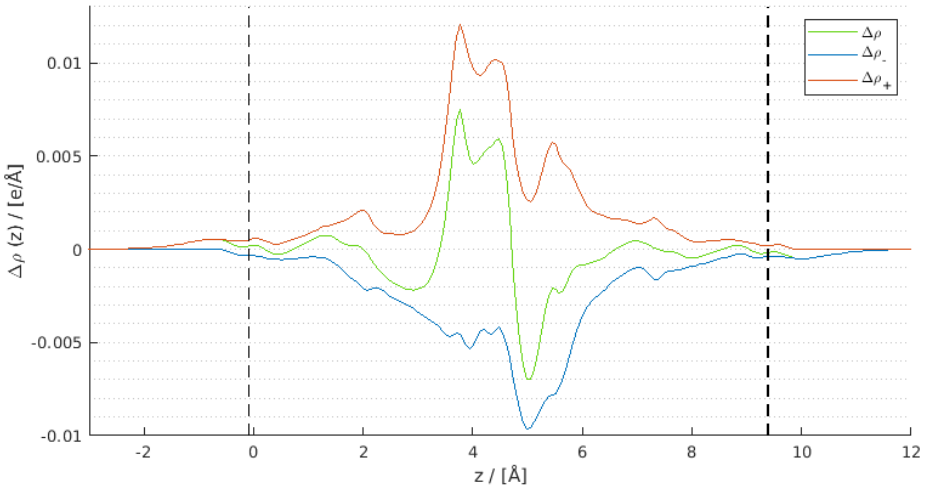

Fig. 2.20: Differential charge density $\Delta\rho(z)$ along the z axis in $H_2O@Li_{24}F_{24}$. The vertical black lines indicate the boundaries of the nanotube.

By integrating the $z \cdot \Delta\rho(z)$ function on the unit cell, one obtains a dipole moment value of 0.17 D, which can be interpreted as the total induced dipole moment due to the rearranged electron density. One can therefore conclude that the dipole-amplification (antiscreening) effect is due, for about 30 % to the deformation of the electronic cloud, while the remaining portion is due to the relative displacements of positive and negative ions (see below).

Distance between the centers of the positive and negative ions

The water molecule encapsulated inside the nanotube interacts with the positive and negative ions, slightly distorting the nanostructure. This effect contributes significantly to the amplifying effect of the electric dipole moment. In order to characterize these distortions we can consider z_+, that is the z component of the charge center of the positive ions Li+, and z_-, the z component of the charge center of the negative ions F-; then we can evaluate $d_\pm = z_+ - z_-$, that is the difference between the z-coordinates of the charge centers of the positive and negative ions. Only the z axis is considered since it has been verified that no significant distortions take place along the x,y directions. The $d_\pm$ quantity is conveniently expressed in mÅ since it is very small compared to the dimensions of the nanotube. One can expect that, for the isolated nanotube, i.e. in the absence of the water molecule ecapsulated inside it, the value of $d_\pm$ is significantly smaller than that computed upon water-molecule encapsulation. The results obtained for $d_{\pm isol}$ of the isolated nanotube are reported in table 2.14, while in table 2.15 we instead report $d_{\pm full}$ for the endohedral complex $H_2O@Li_{24}F_{24}$. Fig. 2.21 and 2.22 describe the behavior of $d_{\pm isol}$ as a function of the unitary cell size and of the kinetic energy cutoff.

$d_{\pm isol}$ [mÅ]		**kinetic energy cutoff** [Ry]						
		40	50	60	70	80	90	100
a [Å]	8	10.98	9.22	9.12	9.22	9.22	9.22	9.22
	9	4.98	2.24	4.40	4.00	3.86	2.13	4.08
	10	0.15	0.33	0.36	0.37	0.24	0.69	0.62
	11	0.84	0.24	0.93	0.32	0.48	0.39	0.21
	12	2.77	0.13	0.52	0.80	0.62	0.37	0.42
	13	2.99	1.25	1.09	0.94	0.49	2.08	0.63
	14	0.89	0.81	0.94	0.44	0.77	0.48	0.71
	15	1.74	0.61	0.88	0.41	0.70	0.62	-

Table 2.14: Distance $d_{\pm isol}$ between positive and negative ions centers in the insolated $Li_{24}F_{24}$ nanotube

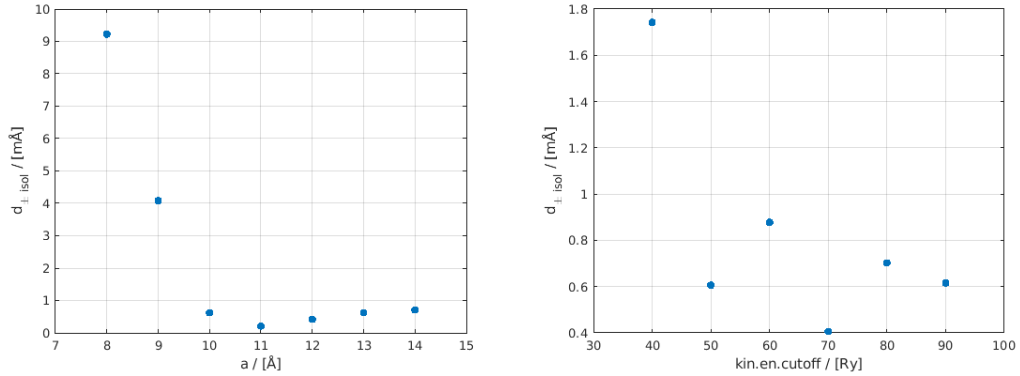

Fig. 2.21: Distance $d_{\pm isol}$ between positive and negative ions centers in the isolated $Li_{24}F_{24}$ nanotube as a function of the the unitary cell size and of the kinetic energy cutoff

$d_{\pm full}$ [mÅ]		**kinetic energy cutoff** [Ry]						
		40	50	60	70	80	90	100
a [Å]	8	6.44	3.99	3.90	3.60	3.73	3.79	3.74
	9	2.97	1.99	1.69	1.48	2.94	2.91	3.08
	10	1.43	1.76	1.78	0.88	1.85	0.84	0.79
	11	0.48	2.61	1.80	2.68	1.97	2.68	1.95
	12	2.74	3.21	2.61	1.05	2.66	1.85	1.86
	13	1.67	1.73	1.91	0.92	1.82	1.85	1.85
	14	1.76	2.51	1.72	1.78	1.75	1.73	1.78
	15	2.06	2.49	1.62	1.74	1.70	1.70	-

Table 2.15: Distance $d_{\pm isol}$ between positive and negative ions centers in the $H_2O@Li_{24}F_{24}$ endohedral complex

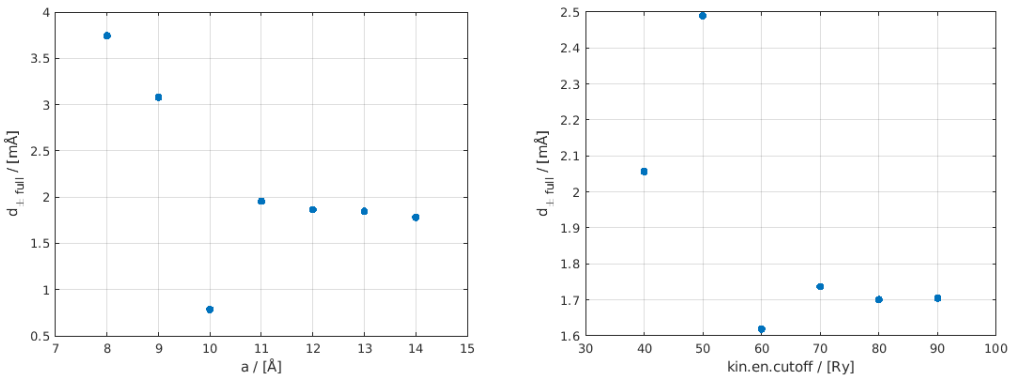

Fig. 2.22: Distance $d_{\pm isol}$ between positive and negative ions centers in the $H_2O@Li_{24}F_{24}$ endohedral complex as a function of the the unitary cell size and of the kinetic energy cutoff

The converged values for $d_{\pm isol}$ turn out to be 0.7 mÅ and 1.7 mÅ for the isolated nanotube and the endohedral complex, respectively. A more detailed description can be obtained (similarly to what done in ref. [14]) by plotting the z-coordinate changes of the ions, upon encapsulation of the water molecule, as a function of the z position of the ions themselves. Since each section of the nanotube has 8 alternating atoms, 4 Li+ ions and 4 F- ions, we consider the average position along z of each of the two quadruplets of ions: z_{+i} for the 4 Li+ ions of the i-th section and z_{-i} for the 4 F- ions of the section i-th. The graph in Fig. 2.23 shows the variation of z_{+i} and z_{-i} upon encapsulation of the water molecule inside the nanotube (the dotted lines are just a guide to the eyes).

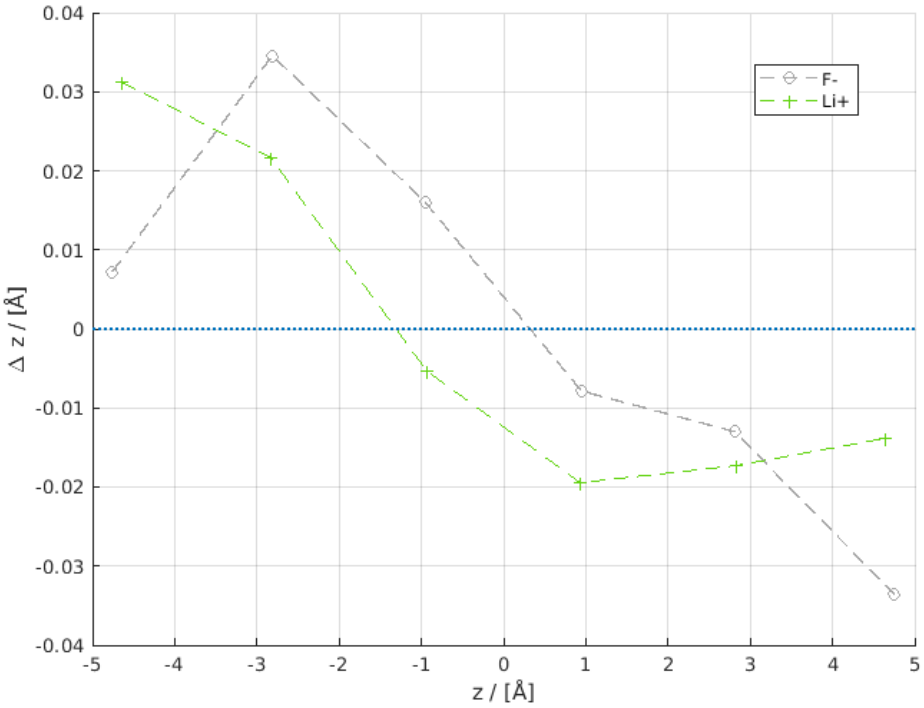

Fig. 2.23: Differential displacements of the positive and negative ions upon encapsulation of the water molecule (see text for details)

2.4 Role of the nanotube's chemical composition

In this section we investigate to what extent the above results about the dielectric properties of the $H_2O@Li_{24}F_{24}$ endohedral complex are modified by changing the composition of the nanotube, namely by replacing Li and F with other alkali-halide atoms. As outlined above we restrict our analysis only to the most stable nanostructures; so, besides $H_2O@Li_{24}F_{24}$, we consider $H_2O@Li_{24}Cl_{24}$, $H_2O@Na_{24}F_{24}$, $H_2O@K_{24}F_{24}$ and $H_2O@K_{24}Cl_{24}$. The calculations were carried out adopting the same approach and technical parameters described in detail for the $H_2O@Li_{24}F_{24}$ endohedral complex; in all the cases the geometry of the nanotube is octagonal with six layers, and the water molecule is located in the center of the nanotube with a dipole moment parallel to the axis of the nanostructure. The results relative to the different considered chemical compositions of the nanotubes are reported in table 2.16. The chemical nature of the nanotube bonds can be described in terms of the so-called ionic character which can be evaluated using the Pauling's relation[39], based on the electronegativity difference between two elements A and B :

$$ion.char. = \left(1 - e^{-\frac{1}{4}(\chi_A - \chi_B)^2}\right) \cdot 100\% \tag{2.3}$$

complex	E_C [eV/at]	E_B [meV]	μ_{isol} [D]	μ_{tot} [D]	$\Delta_{\%}\mu$	$d_{\pm}$ [mÅ]	ion.char.
$H_2O@Li_{24}F_{24}$	-4.2	-225	0.06	2.47	+31 %	1.7	89%
$H_2O@Na_{24}F_{24}$	-3.7	-789	0.12	3.03	+63 %	2.8	90%
$H_2O@K_{24}F_{24}$	-3.6	-954	0.40	3.65	+82 %	8.7	92%
$H_2O@Li_{24}Cl_{24}$	-3.3	-843	0.11	2.49	+33 %	3.9	70%
$H_2O@K_{24}Cl_{24}$	-2.9	-794	1.55	5.12	+100%	19.9	75%

Table 2.16: Cohesive energy, E_C, and dipole moment, μ_{isol}, of the isolated nanotube, binding energy, E_B, dipole moment, μ_{tot}, induced dipole moment $\Delta_{\%}\mu$, distance $d_{\pm isol}$ between positive and negative ions centers, and ionic character of different considered endohedral complexes

It is interesting to compare the present results to those obtained in previous investigations on encapsulation of a water molecule inside fullerene-like nanocages[14]. Remarkably, the amplification of the dipole moment in the $H_2O@Li_{24}F_{24}$ endohedral structure turns out to be twice than that (+18%) found in the $H_2O@Li_{36}F_{36}$ nanocage [14]. Such an increase of the antiscreening effect, with respect to that observed in the corresponding nanocage structures, is also found in $H_2O@Na_{24}F_{24}$ (+63% dipole amplification against +44% for the nanocage) and in $H_2O@Li_{24}Cl_{24}$ (+33% against +25%). Note that the effect is particularly pronounced in $H_2O@K_{24}Cl_{24}$ (for these endohedral structure no comparison with the corresponding endohedral nanocage is available) since the dipole amplification factor (+100%) shows that the antiscreening behavior is quite strong since the induced dipole moment is twice that of the isolated molecule.Also note

that the distances between positive and negative ions are larger compared to the corresponding values computed in the nanocages[14] This observation further supports the conclusion that the differential displacement of the positive and negative ions is the main source of the peculiar antiscreening effect.

The results for the endohedral stuctures containing K atoms deserve a comment. In fact, by adopting the same supercell parameters used in the other cases, one finds that the dipole moment of these structures, without the encapsulated water molecule, μ_{isol}, does not vanish, differently from the other nanostructures. We have therefore checked if this finding could be ascribed to an insufficient convergence of μ_{isol} as a function of the simulation cell. Data of table 2.17 suggest a relation between the percent occupied volume of the unit cell, with standard dimensions a=12.5 Å and c=25 Å, and the isolated nanotube dipole moment μ_{isol}.

complex	diameter [Å]	length [Å]	$V_{\%}$	μ_{isol} [D]
$H_2O@Li_{24}F_{24}$	4.7	9.4	4 %	0.06
$H_2O@Na_{24}F_{24}$	5.6	11.0	7 %	0.12
$H_2O@K_{24}F_{24}$	6.3	12.7	10 %	0.40
$H_2O@Li_{24}Cl_{24}$	6.0	12.0	9 %	0.11
$H_2O@K_{24}Cl_{24}$	7.7	15.0	18 %	1.55

Table 2.17: Nanotube diameter, length (along z), percent occupied volume in the unit cell with a=12.5 Å and c=25 Å, $V_{\%}$, and dipole moment of the isolated nanotube

We have therefore repeated the structural optimization of the two larger isolated nanotubes $K_{24}F_{24}$ and $K_{24}Cl_{24}$ by adopting a larger unit cell with dimensions a=15 Å and c=30 Å (in place of the original ones a=12.5 Å and c=25 Å). The computed dipole moment of the two structures is significantly reduced in the larger unit cell: for $K_{24}F_{24}$ it decrease from 0.4 D (a=12.5 Å) to 0.28 D (a=15 Å), while for $K_{24}Cl_{24}$ it decrease from 1.55 D (a=12.5 Å) to 0.42 D (a=15 Å). Although we do not expect that the qualitative conclusion about the dipole amplification (antiscreening effect) characterizing these endohedral structures is affected by these findings, nonetheless they suggest that more accurate, quantitative results can be only obtained for the largest considered endohedral nanotubes by adopting larger unit cells (implying considerably higher computational costs).

2.5 Role of the size of the nanotube

In this section we investigate the role of the size of the nanotube by focusing on lithium fluoride nanostructures of different geometries, considering two different kinds of sections (octagonal and dodecagonal) of the nanotube section and different numbers of layers. The hexagonal section is not taken into account because the corresponding nanotube would be too small to encapsulate a water molecule without severely distorting the nanostructure. Similarly, the decagonal section, that would be intermediate between the octagonal and the dodecagonal one, is not considered since the resulting endohedral structure turns out to be unstable. Concerning the number of layers, besides the 6 layers assumed in the previous applications, we also considered 5 and 7 layers. Again the calculations were carried out adopting the same approach and technical parameters used for the reference $H_2O@Li_{24}F_{24}$ endohedral complex. The results are reported in tables 2.18 and 2.19.

complex	section	n.layers	E_C [eV/at]	E_B [meV]	μ_{isol} [D]	μ_{tot} [D]
$H_2O@Li_{20}F_{20}$	octagonal	5	-4.22	-193	0.07	2.07
$H_2O@Li_{24}F_{24}$	octagonal	6	-4.23	-226	0.10	2.39
$H_2O@Li_{28}F_{28}$	octagonal	7	-4.24	-228	0.02	2.36
$H_2O@Li_{30}F_{30}$	dodecagonal	5	-4.22	-578	0.04	1.37
$H_2O@Li_{36}F_{36}$	dodecagonal	6	-4.23	-516	0.05	1.12
$H_2O@Li_{42}F_{42}$	dodecagonal	7	-4.24	-265	0.06	1.28

Table 2.18: Cohesive energy, E_C, and dipole moment, μ_{isol}, of the isolated nanotube, binding energy, E_B and dipole moment, μ_{tot} of the endohedral complexes (see text for details)

complex	section	n.layers	$\Delta_{\%}\mu$	$d_{\pm\, isol}$ [mÅ]	$d_{\pm\, tot}$ [mÅ]
$H_2O@Li_{20}F_{20}$	octagonal	5	+12%	0.0	3.1
$H_2O@Li_{24}F_{24}$	octagonal	6	+29%	0.0	1.8
$H_2O@Li_{28}F_{28}$	octagonal	7	+31%	0.0	1.8
$H_2O@Li_{30}F_{30}$	dodecagonal	5	-26%	0.0	-5.0
$H_2O@Li_{36}F_{36}$	dodecagonal	6	-40%	0.0	-4.6
$H_2O@Li_{42}F_{42}$	dodecagonal	7	-32%	0.0	-1.8

Table 2.19: Percent induced dipole moment $\Delta_{\%}\mu$, induced dipole due to the rearranging of electron density $\mu_{ind-e.}$, distance $d_{\pm\, tot}$ between positive and negative ions centers of the isolated nanotube, $d_{\pm\, isol}$, and of the endohedral complexes , $d_{\pm\, tot}$ (see text for details)

As can be seen, considering lithium-fluoride endohedral structures with octagonal section, the percent amplification of the dipole moment $\Delta\mu_{\%}$ increases with the number of layers, which can be explained by the more effective collective effect of a larger number of ions of opposite charge in inducing an amplification of the dipole moment. Interestingly, lithium-fluoride endohedral structures with the dodecagonal section, differently from those with the octagonal one, exhibit a clear screening effect since the total-dipole moment is reduced with respect to that of the

isolated water molecule. In this case the endohedral structure is characterized by a significant deformation in the transversal direction (see Fig. 2.24).

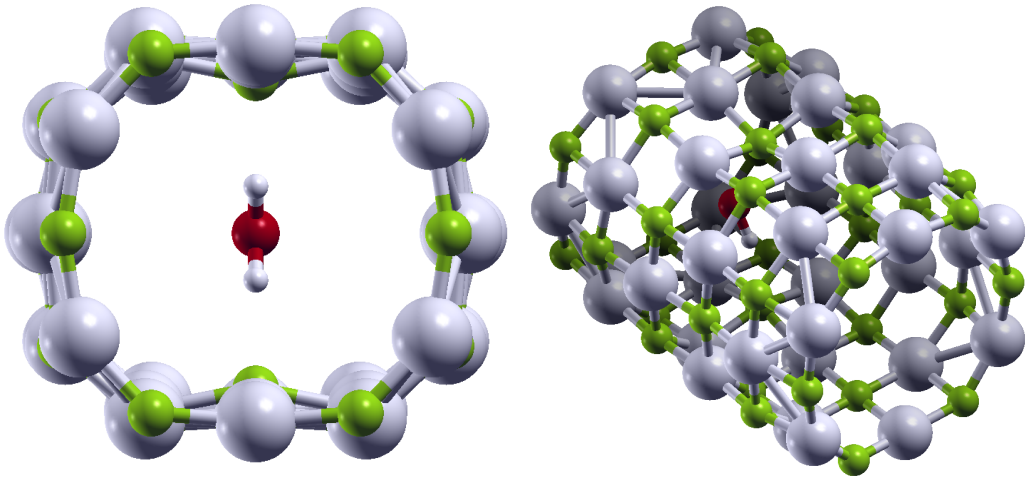

Fig. 2.24: Two views of the $H_2O@Li_{36}F_{36}$ nanotube with lithium-fluoride dodecagonal section and 6 layers.

The possibility of switching from antiscreening to screening effect in alkali-halide nanostructures by just changing the nanotube's section is remarkable and clearly deserves further analysis. As done previously, the differential charge density $\Delta\rho(\vec{r})$ was calculated for the endohedral complex $H_2O@Li_{36}F_{36}$ with dodecagonal section and six layers. Fig. 2.25 compares the differential charge density of two different nanotubes: octagonal with six layers $H_2O@Li_{24}F_{24}$, and dodecagonal, again with six layers $H_2O@Li_{36}F_{36}$. The red (blue) surface denotes electron density gain (loss) regions. For both the nanotubes the plotted isosurfaces correspond to values of $\pm 15 \cdot 10^{-3}\, e/\text{Å}^3$.

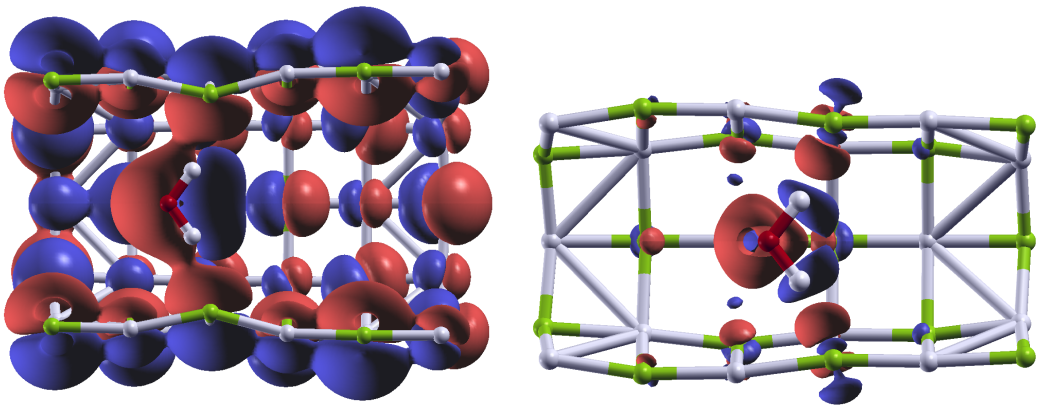

Fig. 2.25: Differential charge density comparison between $H_2O@Li_{24}F_{24}$ octagonal nanotube with six layers (on the right) and $H_2O@Li_{36}F_{36}$ dodecagonal nanotube with six layers (on the left)

In both the endohedral complexes one can appreciate an electron density gain around the Oxigen atom and a loss around the two Hydrogen atoms of the water molecule. The dodecagonal

nanotube, differently from the octagonal one, turns out to be characterized by a rearrangement of the electron density around Lithium and Fluorine pairs in such a way to generate dipole moments opposite to that of the encapsulated water molecule, thus explaining the observed screening behavior. Also in this case the screening effect can be analysed by calculating the differential electron density along z axis $\Delta\rho(z)$, plotted in Fig. 2.26.

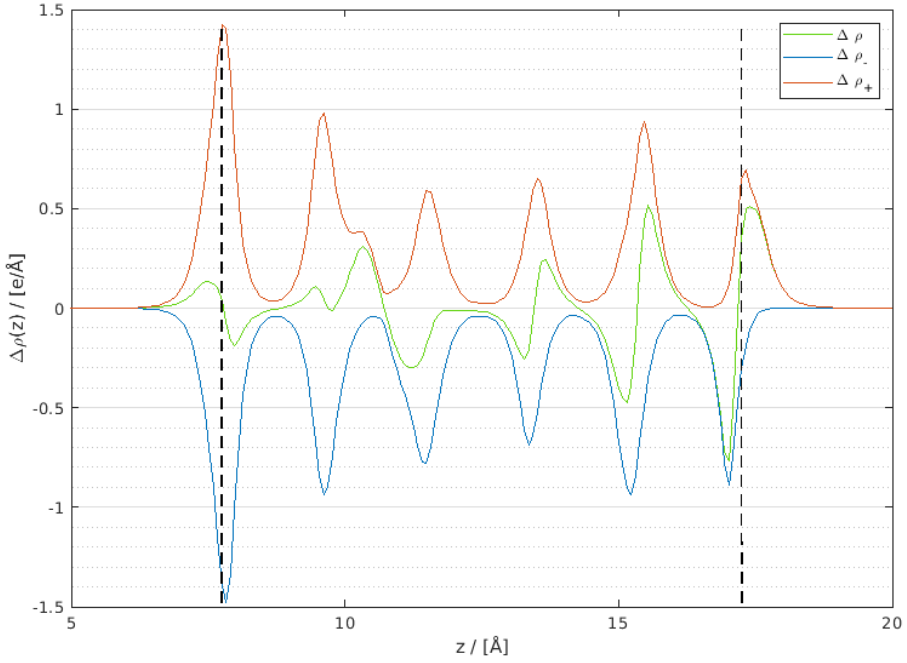

Fig. 2.26: Differential charge density $\Delta\rho(z)$ along the z axis in $H_2O@Li_{36}F_{36}$. The vertical black lines indicate the boundaries of the nanotube.

By integrating the $z \cdot \Delta\rho(z)$ function over the unit cell, one obtains a dipole moment value of -0.6 D (opposite to that of the water molecule), which can be interpreted as the total induced dipole moment due to the rearranged electron density. In trying to better elucidate the role of the ion positions and particularly of the specific adopted nanotube's structure and section, one can also compute the angular induced dipole moment $\mu_{ind}(\theta)$ (Fig. 2.27) To obtain this quantity, we first performed a coordinate transformation of the differential electron density from Cartesian to cylindrical coordinates, $\Delta\rho(x, y, z) \rightarrow \Delta\rho(r, \theta, z)$. Then, the function $z \cdot \Delta\rho(r, \theta, z)$ was integrated over r and z in the unit cell, $\mu_{ind}(\theta) = \int_{\text{cell}} dr\, dz\, z\Delta\rho(r, \theta, z)$.

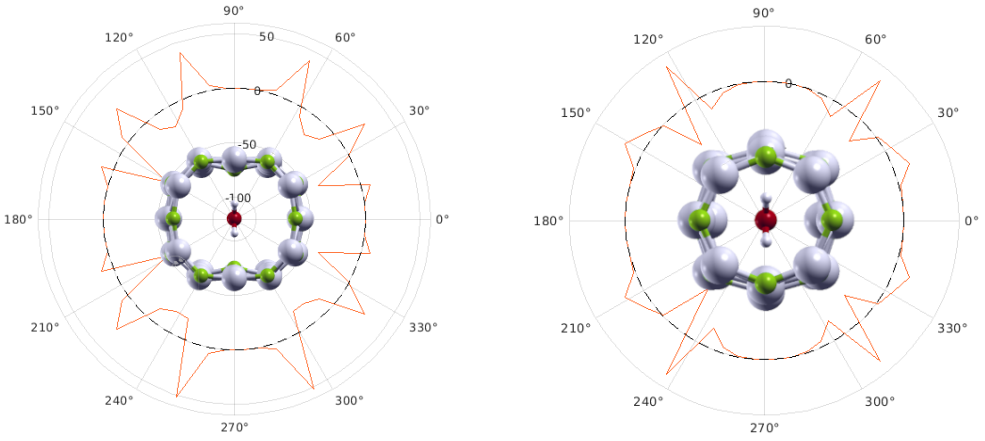

Fig. 2.27: Angular induced dipole moment $\mu_{ind}(\theta)$, for two endohedral structures: dodecagonal nanotube $H_2O@Li_{36}F_{36}$ (left) and octagonal nanotube $H_2O@Li_{24}F_{24}$ (right), both with six layers. The dotted, circular black line represents the zero-value level

The behavior of this function is clearly different in the two considered endohedral nanostructures. In fact, in the dodecagonal nanotube one can observe pronounced negative contributions, mostly localized at eight different angles: 30° , 60°, 120°, 150°, 210°, 240°, 300° and 330°, while instead, in the the octagonal nanotube negative contributions are only localized at four angles: 45°, 135°, 225° and 315°. More detailed analysis shows that these negative contributions are localized at angles where one can find atoms of the nanotube that are neither on the plane containing the water molecule neither on the one orthogonal to it; these atoms are four for each layer in the octagonal nanotube, while instead eight for each layer in the dodecagonal nanotube.

The dipole moment component related to the positive and negative ions displacement has been studied for the dodecagonal nanotube $H_2O@Li_{36}F_{36}$ too. Fig.2.28 shows the relative displacements in the two cases, dodecagonal (left) and octagonal (right). Significant differences are evident. From one hand in the the octagonal nanotube the displacements are almost double than in the dodecagonal one. From the other in the dodecagonal nanotube case thee green curve (Li+ ions) is relatively lower than the grey one (F- ions). As a consequence, the Li+ ions displacements are on average smaller than the F- ones, and so the overall distance between positive and negative ions centers along z is negative $d_{\pm\, tot} = -4.6\, m$Å. Such a negative value of $d_{pm\, tot}$ means that the ions displacement induces a further screening effect in the dodecagonal nanotube, contrary to the octagonal case in which instead the ions displacement contributes significantly to the dipole moment amplification.

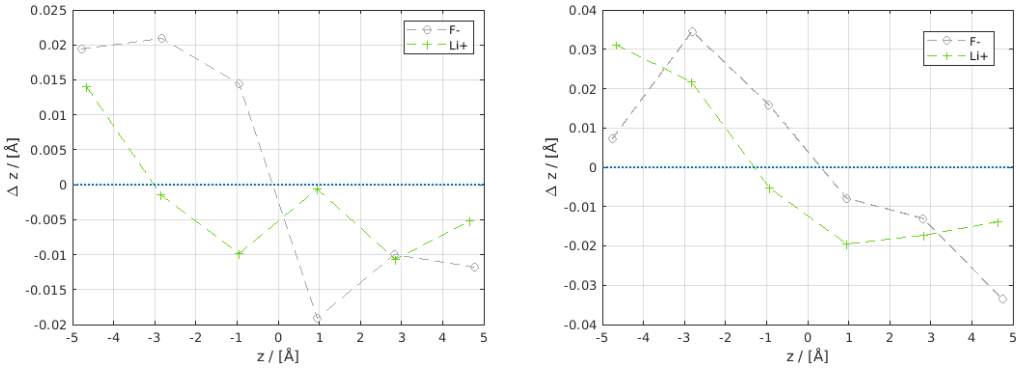

Fig. 2.28: Differential displacements of the positive and negative ions upon encapsulation of the water molecule into the dodecagonal nanotube $H_2O@Li_{36}F_{36}$ (left) and into the octagonal nanotube $H_2O@Li_{24}F_{24}$ (right)

2.6 Role of the specific encapsulated molecule: NaF and LiF in place of H_2O

Finally, we have verified the effect of replacing, as the molecule encapsulated inside $Li_{24}F_{24}$, water by other polar molecules, in particular NaF and LiF, which are linear molecules characterized by a dipole moment even greater than that of H_2O. The results are reported in table 2.20.

complex	E_B [meV]	μ_{mol} [D]	μ_{tot} [D]	$\Delta_{\%}\mu$	$d_{\pm}$ [mÅ]	ion.char.
$H_2O@Li_{24}F_{24}$	-225	1.8	2.4	+31 %	1.8	32 %
$LiF@Li_{24}F_{24}$	-2328	6.1	5.2	-16 %	19.8	89 %
$NaF@Li_{24}F_{24}$	-2158	7.8	6.7	-16 %	19.8	90 %

Table 2.20: Cohesive energy, E_C, dipole moment, μ_{mol}, of the isolated encapsulated molecule, binding energy, E_B, dipole moment, μ_{tot}, induced dipole moment $\Delta_{\%}\mu$, distance $d_{\pm isol}$ between positive and negative ions centers, and ionic character considering different molecules encapsulated in $Li_{24}F_{24}$

As can be seen the binding energies of the $NaF@Li_{24}F_{24}$ and $LiF@Li_{24}F_{24}$ endohedral nanostructures are much larger (one order of magnitude) in absolute value than that relative to $H_2O@Li_{24}Cl_{24}$. This suggests that one or more true chemical bonds are actually formed between the encapsulated molecule and the surrounding nanotube. This is qualitatively confirmed by inspection of Fig. 2.29. $NaF@Li_{24}F_{24}$ and $LiF@Li_{24}F_{24}$ show a moderate screening effect, however the comparison with the dielectric properties of the reference $H_2O@Li_{24}Cl_{24}$ nanostructure is not completely meaningful in view of the fact that $F@Li_{24}F_{24}$ and $LiF@Li_{24}F_{24}$ cannot be certainly described in terms of encapsulated molecules weakly interacting with the surrounding nanotube.

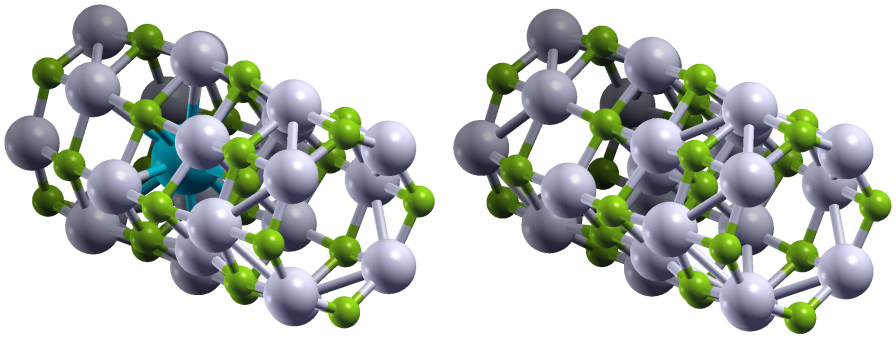

Fig. 2.29: $NaF@Li_{24}F_{24}$ and $LiF@Li_{24}F_{24}$ endohedral structures

Chapter 3

Conclusions

This thesis work reports the results of a first-principles investigation of alkali-halide nanotubes with particular emphasis on their dielectric properties. In particular, we have considered, as the most promising systems, nanotubes with octagonal transversal section and six layers in the longitudinal direction. As a preliminary step the stability of nanotubes made by different binary combinations of alkali metals and halides has been investigated, finding that the Lithium-Fluoride (LiF) nanotube is the most stable one. Next we have investigated, by first-principles techniques based on the DFT (using a state-of-the art approach able to properly describe also long-range van der Waals interactions), the properties of endohedral alkali-halide nanotubes obtained by encapsulation of a water molecule, similarly to what done in previous applications to alkali-halide, fullerene-like nanocages. Extended tests have been carried out to verify the accurate convergence of the basic structural, energetic, and dielectric properties of the system. In the most stable $H_2O@Li_{24}F_{24}$ endohedral complex an evident antiscreening effect is observed since there is a substantial amplification (about 30%) of the dipole moment with respect to that of the isolated water molecule. In this structure the energetically favored configuration is the one where the water molecule is located in the center of the nanotube with its dipole moment parallel to the axis of the nanotube. A detailed investigation has been performed to elucidate the antiscreening effect by computing both the differential electron density distribution and profile, and the relative displacements of positive and negative ions of the nanotubes. In this way one can conclude that the induced dipole moment is mostly due just to the rearrangement of the ions. Interestingly, these results are qualitatively and semi-quantitatively similar to those previously obtained in the study of endohedral alkali-halide (fullerene-like) nanocages[14], as can be deduced looking at table 3.1, which summarizes the basic quantities characterizing the $H_2O@Li_{36}F_{36}$ and $H_2O@Li_{24}F_{24}$ nanostructures.

	fullerene-like nanocage $H_2O@Li_{36}F_{36}$	nanotube $H_2O@Li_{24}F_{24}$
Nanostructure diameter	9.4 Å	4.6 Å
Cohesive energy	-3.2 eV/atom	-4.2 eV/atom
Binding energy	-152 meV	-225 meV
Percent induced dipole moment	+18 %	+31 %

Table 3.1: Comparison of basic quantities characterizing the $H_2O@Li_{36}F_{36}$ and $H_2O@Li_{24}F_{24}$ nanostructures

The detailed reaction path corresponding to the encapsulation of the water molecule in the $Li_{24}F_{24}$ nanotube has been also reproduced, using the NEB approach, with an estimate of the related energy barrier (about 0.6 eV). Besides $H_2O@Li_{24}F_{24}$, other endohedral nanostructures with an encapsulated water molecule have been investigated, considering the most stable alkail-halide nanotubes, always with octagonal section and 6 layers: $H_2O@Li_{24}Cl_{24}$, $H_2O@Na_{24}F_{24}$, $H_2O@K_{24}F_{24}$, and $H_2O@K_{24}Cl_{24}$. In these other systems the antiscreening phenomenon is even more pronounced that in $H_2O@Li_{24}F_{24}$: in fact the dipole amplification is estimated to be +63%, +82%, +33% and +100%, respectively. We have also verified that the antiscreening effect in alkali-halide nanotubes with octagonal transversal sections increases as a function of the number of layers in the longitudinal direction. Interestingly, the specific geometric structure of the nanotube seems to be crucial for triggering the antiscreening phenomenon. In fact, calculations on the alternative $H_2O@Li_{36}F_{36}$ endohedral nanostructure with dodecagonal section (instead of octogonal) indicate a reduction of the total dipole moment, so that a screening behavior similar to that observed in more conventional carbon nanocages is observed. Finally, we have also studied endohedral $Li_{24}F_{24}$ nanostructures where the encapsulated water molecule is replaced by linear, ionic-bonded molecules, NaF and LiF having a dipole moment even larger that that of the water molecule. In this case a moderate screening effect is observed, however the strong interaction (large binding energy) between encapsulated molecules and nanotube suggests that the whole structure is significantly altered with the formation of new genuine chemical bonds.

Appendix A

Quantum-ESPRESSO input parameters

In table A.1 a detailed list of all the typical parameters used for running the "pw.x" Quantum-ESPRESSO program is reported:

Parameter	Single atom	Structure
calculation	scf	scf/relax
ibrav	6	6
A	8 ÷ 15	8 ÷ 15
C	16 ÷ 30	16 ÷ 30
ecutwfc	40 ÷ 100	40 ÷ 100
ecutrho	240 ÷ 600	240 ÷ 600
occupations	smearing	smearing
smearing	f-d	f-d
degauss	0.01	0.01
input_dft	rvv10	rvv10
nspin	2	N.D.
starting_magnetization	0.5	N.D.
conv_thr	10^{-8}	10^{-8}
mixing_beta	0.57	0.57
mixing_mode	plain	plain
K_POINTS	automatic 1 1 1 0 0 0	automatic 1 1 1 0 0 0

Table A.1: Parameters used in pw.x code

The "pp.x" post-processin program was used to obtain the electron density function and the electron density differential displacement. The main settings were : "plot_num=0", "iflag=3" and "output_format=5".

Table A.2 reports information about the pseudopotential approach, including the number of considered valence electrons and the suggested minimum kinetic energy cutoff, both for the wavefunction and the electron density expansions.

Element	Z_i [-]	Pseudopotential name	min. **ecutwfc**	min. **ecutrho**
H	1	H.pbe-rrkjus_psl.1.0.0.UPF	46 Ry	221 Ry
Li	3	Li.pbe-sl-rrkjus_psl.1.0.0.UPF	50 Ry	325 Ry
O	6	O.pbe-n-rrkjus_psl.1.0.0.UPF	47 Ry	323 Ry
F	7	F.pbe-n-rrkjus_psl.1.0.0.UPF	49 Ry	316 Ry
Na	9	Na.pbe-spn-rrkjus_psl.1.0.0.UPF	66 Ry	323 Ry
Cl	7	Cl.pbe-n-rrkjus_psl.1.0.0.UPF	45 Ry	223 Ry
K	9	K.pbe-spn-rrkjus_psl.1.0.0.UPF	41 Ry	277 Ry
Br	7	Br.pbe-n-rrkjus_psl.1.0.0.UPF	49 Ry	196 Ry

Table A.2: Data about the pseudopotentials used

Appendix B

CloudVeneto

A central element of this thesis are the DFT simulations with Quantum-ESPRESSO. These simulations range from simple self-consistent "scf" electonic optimizations, which can take minutes to complete, up to more demanding, structural optimization simulations lasting 8 or more hours, with RAM memory use of up to 20 GB . The preliminary study phase and the convergence study required several dozen structural optimizations, with a considerable computational effort. In order to be able to carry it out easily, it was necessary to look for a computing platform suitable for these needs. The platform used was CloudVeneto, an initiative involving 10 departments of the University of Padua, the Padua division of INFN (national institute of nuclear physics) and the INFN national laboratories of Legnaro. Upon request, an account was assigned with the following available resources: 200 GB of storage memory, 20 Intel 2.5 GHz virtual CPUs and 20 GB of RAM memory. To make optimal use of the available computational resources, two virtual machines have been instantiated, each with the Ubuntu 22.04.2 LTS operating system and two different "flavours": the first for the heavier simulations of structural optimization, operating with an extra large flavor "cloudveneto.xlarge" having 8 virtual CPUs and 16 GB of RAM, the second instead dedicated to more numerous and less demanding simulations such as single point simulations of self-consistency "scf", operating with a medium flavor "cloudveneto.medium" with 2 virtual CPUs and 4GB of RAM. Since this project does not belong directly to the INFN group, an SSH tunnel through an intermediate gate has been made mandatory for access to the virtual machines in order to guarantee IT security. In order to optimize the use of the machines in time and to complete the numerous simulations in a reasonable time, the generation of the input files and the storage of the output files has been automated through suitably designed bash scripts.

Bibliography

[1] A. K. Geim and K. S. Novoselov. "The rise of graphene". In: *Nature Materials* 6.3 (Mar. 2007), pp. 183–191. ISSN: 1476-4660. DOI: 10.1038/nmat1849. URL: https://doi.org/10.1038/nmat1849.

[2] Max Lemme. "Current Status of Graphene Transistors". In: *Solid State Phenomena* 156-158 (Nov. 2009). DOI: 10.4028/www.scientific.net/SSP.156-158.499.

[3] H.W.Kroto et al. "C60: Buckminsterfullerene". In: *Nature* 318 (1985). DOI: 10.1038/318162a0. URL: https://doi.org/10.1038/318162a0.

[4] Takeshi Akasaka and Shigeru Nagase. *Endofullerenes: A New Family of Carbon Clusters*. Jan. 2002. ISBN: 978-90-481-6159-1. DOI: 10.1007/978-94-015-9938-2.

[5] Aleksander Jaworski and Niklas Hedin. "Local energy decomposition analysis and molecular properties of encapsulated methane in fullerene (CH4@C60)". In: *Phys. Chem. Chem. Phys.* 23 (38 2021), pp. 21554–21567. DOI: 10.1039/D1CP02333K. URL: http://dx.doi.org/10.1039/D1CP02333K.

[6] Tomohiro Suetsuna et al. "Separation of N2@C60 and N@C60". In: *Chemistry (Weinheim an der Bergstrasse, Germany)* 8 (Mar. 2003), pp. 5079–83. DOI: 10.1002/1521-3765(20021115)8:22<5079::AID-CHEM5079>3.0.CO;2-H.

[7] Koichi Komatsu, Michihisa Murata, and Yasujiro Murata. "Encapsulation of Molecular Hydrogen in Fullerene C60 by Organic Synthesis". In: *Science* 307.5707 (2005), pp. 238–240. DOI: 10.1126/science.1106185. eprint: https://www.science.org/doi/pdf/10.1126/science.1106185. URL: https://www.science.org/doi/abs/10.1126/science.1106185.

[8] Kei Kurotobi and Yasujiro Murata. "A Single Molecule of Water Encapsulated in Fullerene C60". In: *Science* 333.6042 (2011), pp. 613–616. DOI: 10.1126/science.1206376. eprint: https://www.science.org/doi/pdf/10.1126/science.1206376. URL: https://www.science.org/doi/abs/10.1126/science.1206376.

[9] Sally Bloodworth et al. “First Synthesis and Characterization of CH4@C60”. In: *Angewandte Chemie International Edition* 58 (Feb. 2019), pp. 5038–5043. DOI: 10.1002/anie.201900983.

[10] C.N. Ramachandran and N. Sathyamurthy. “Water clusters in a confined nonpolar environment”. In: *Chemical Physics Letters* 410.4 (2005), pp. 348–351. ISSN: 0009-2614. DOI: https://doi.org/10.1016/j.cplett.2005.04.113. URL: https://www.sciencedirect.com/science/article/pii/S0009261405006469.

[11] Bernd Ensing, Francesca Costanzo, and Pier Luigi Silvestrelli. “On the Polarity of Buckminsterfullerene with a Water Molecule Inside”. In: *The Journal of Physical Chemistry A* 116.49 (2012). PMID: 23157158, pp. 12184–12188. DOI: 10.1021/jp311161q. eprint: https://doi.org/10.1021/jp311161q. URL: https://doi.org/10.1021/jp311161q.

[12] Orlando Carrillo-Bohórquez, Álvaro Valdés, and Rita Prosmiti. “Encapsulation of a Water Molecule inside C60 Fullerene: The Impact of Confinement on Quantum Features”. In: *Journal of Chemical Theory and Computation* 17.9 (2021). PMID: 34420292, pp. 5839–5848. DOI: 10.1021/acs.jctc.1c00662. eprint: https://doi.org/10.1021/acs.jctc.1c00662. URL: https://doi.org/10.1021/acs.jctc.1c00662.

[13] Francisco A. Fernandez-Lima et al. “Alkali Halide Nanotubes: Structure and Stability”. In: *The Journal of Physical Chemistry C* 116.8 (2012), pp. 4965–4969. DOI: 10.1021/jp208090j. eprint: https://doi.org/10.1021/jp208090j. URL: https://doi.org/10.1021/jp208090j.

[14] Pier Luigi Silvestrelli et al. “Screening and antiscreening in fullerene-like cages: Dipole-field amplification with ionic nanocages”. In: *Carbon Trends* 10 (2023), p. 100242. ISSN: 2667-0569. DOI: https://doi.org/10.1016/j.cartre.2022.100242. URL: https://www.sciencedirect.com/science/article/pii/S2667056922000980.

[15] Paolo Giannozzi et al. “QUANTUM ESPRESSO: a modular and open-source software project for quantum simulations of materials”. In: *Journal of Physics: Condensed Matter* 21.39 (Sept. 2009), p. 395502. DOI: 10.1088/0953-8984/21/39/395502. URL: https://doi.org/10.1088%5C%2F0953-8984%5C%2F21%5C%2F39%5C%2F395502.

[16] V. Mussi et al. “Surface nanostructuring and optical activation of lithium fluoride crystals by ion beam irradiation”. In: *Applied Physics Letters* 88.10 (Mar. 2006). 103116. ISSN: 0003-6951. DOI: 10.1063/1.2177660. eprint: https://pubs.aip.org/aip/apl/article-pdf/doi/10.1063/1.2177660/13244458/103116_1_online.pdf. URL: https://doi.org/10.1063/1.2177660.

[17] F H Wang et al. “Strengthening of glass rods and bottles with water based epoxy acrylate coatings”. In: *Materials science and technology* 13.2 (Feb. 1997). ISSN: 0267-0836.

[18] Youngkyoo Kim. “Power-law-type electron injection through lithium fluoride nanolayers in phosphorescence organic light-emitting devices”. In: *Nanotechnology* 19.35 (July 2008), p. 355207. DOI: 10.1088/0957-4484/19/35/355207. URL: https://dx.doi.org/10.1088/0957-4484/19/35/355207.

[19] P. Hohenberg and W. Kohn. “Inhomogeneous Electron Gas”. In: *Phys. Rev.* 136 (3B Nov. 1964), B864–B871. DOI: 10.1103/PhysRev.136.B864. URL: https://link.aps.org/doi/10.1103/PhysRev.136.B864.

[20] G. Vignale and Mark Rasolt. “Density-functional theory in strong magnetic fields”. In: *Phys. Rev. Lett.* 59 (20 Nov. 1987), pp. 2360–2363. DOI: 10.1103/PhysRevLett.59.2360. URL: https://link.aps.org/doi/10.1103/PhysRevLett.59.2360.

[21] Mel Levy. “Universal variational functionals of electron densities, first-order density matrices, and natural spin-orbitals and solution of the v-representability problem”. In: *Proceedings of the National Academy of Sciences* 76.12 (1979), pp. 6062–6065. DOI: 10.1073/pnas.76.12.6062. eprint: https://www.pnas.org/doi/pdf/10.1073/pnas.76.12.6062. URL: https://www.pnas.org/doi/abs/10.1073/pnas.76.12.6062.

[22] W. Kohn and L. J. Sham. “Self-Consistent Equations Including Exchange and Correlation Effects”. In: *Phys. Rev.* 140 (4A Nov. 1965), A1133–A1138. DOI: 10.1103/PhysRev.140.A1133. URL: https://link.aps.org/doi/10.1103/PhysRev.140.A1133.

[23] Narbe Mardirossian et al. “Use of the rVV10 Nonlocal Correlation Functional in the B97M-V Density Functional: Defining B97M-rV and Related Functionals”. In: *The Journal of Physical Chemistry Letters* 8.1 (2017). PMID: 27936759, pp. 35–40. DOI: 10.1021/acs.jpclett.6b02527. eprint: https://doi.org/10.1021/acs.jpclett.6b02527. URL: https://doi.org/10.1021/acs.jpclett.6b02527.

[24] Oleg A. Vydrov and Troy Van Voorhis. “Nonlocal van der Waals density functional: The simpler the better”. In: *The Journal of Chemical Physics* 133.24 (Dec. 2010). 244103. ISSN: 0021-9606. DOI: 10.1063/1.3521275. eprint: https://pubs.aip.org/aip/jcp/article-pdf/doi/10.1063/1.3521275/13569567/244103_1_online.pdf. URL: https://doi.org/10.1063/1.3521275.

[25] Kyuho Lee et al. “Higher-accuracy van der Waals density functional”. In: *Phys. Rev. B* 82 (8 Aug. 2010), p. 081101. DOI: 10.1103/PhysRevB.82.081101. URL: https://link.aps.org/doi/10.1103/PhysRevB.82.081101.

[26] John P. Perdew, Kieron Burke, and Matthias Ernzerhof. "Generalized Gradient Approximation Made Simple". In: *Phys. Rev. Lett.* 77 (18 Oct. 1996), pp. 3865–3868. DOI: 10.1103/PhysRevLett.77.3865. URL: https://link.aps.org/doi/10.1103/PhysRevLett.77.3865.

[27] Haowei Peng et al. "Versatile van der Waals Density Functional Based on a Meta-Generalized Gradient Approximation". In: *Physical Review X* 6.4 (Oct. 2016). DOI: 10.1103/physrevx.6.041005. URL: https://doi.org/10.1103%5C%2Fphysrevx.6.041005.

[28] Guillermo Romá n-Pérez and José M. Soler. "Efficient Implementation of a van der Waals Density Functional: Application to Double-Wall Carbon Nanotubes". In: *Physical Review Letters* 103.9 (Aug. 2009). DOI: 10.1103/physrevlett.103.096102. URL: https://doi.org/10.1103%5C%2Fphysrevlett.103.096102.

[29] Éamonn D. Murray, Kyuho Lee, and David C. Langreth. "Investigation of Exchange Energy Density Functional Accuracy for Interacting Molecules". In: *Journal of Chemical Theory and Computation* 5.10 (2009). PMID: 26631788, pp. 2754–2762. DOI: 10.1021/ct900365q. eprint: https://doi.org/10.1021/ct900365q. URL: https://doi.org/10.1021/ct900365q.

[30] Riccardo Sabatini, Tommaso Gorni, and Stefano de Gironcoli. "Nonlocal van der Waals density functional made simple and efficient". In: *Physical Review B* 87 (Jan. 2013). DOI: 10.1103/PhysRevB.87.041108.

[31] M. Born and R. Oppenheimer. "Zur Quantentheorie der Molekeln". In: *Annalen der Physik* 389.20 (1927), pp. 457–484. DOI: https://doi.org/10.1002/andp.19273892002. eprint: https://onlinelibrary.wiley.com/doi/pdf/10.1002/andp.19273892002. URL: https://onlinelibrary.wiley.com/doi/abs/10.1002/andp.19273892002.

[32] Gianluca Prandini et al. "Precision and efficiency in solid-state pseudopotential calculations". In: *npj Computational Materials* 4.1 (2018). http://materialscloud.org/sssp, p. 72. ISSN: 2057-3960. DOI: 10.1038/s41524-018-0127-2. URL: https://www.nature.com/articles/s41524-018-0127-2.

[33] David Vanderbilt. "Soft self-consistent pseudopotentials in a generalized eigenvalue formalism". In: *Phys. Rev. B* 41 (11 Apr. 1990), pp. 7892–7895. DOI: 10.1103/PhysRevB.41.7892. URL: https://link.aps.org/doi/10.1103/PhysRevB.41.7892.

[34] Kurt Lejaeghere et al. "Reproducibility in density functional theory calculations of solids". In: *Science* 351.6280 (2016), aad3000. DOI: 10.1126/science.aad3000. eprint: https://www.science.org/doi/pdf/10.1126/science.aad3000. URL: https://www.science.org/doi/abs/10.1126/science.aad3000.

[35] Felix Bloch. "Über die Quantenmechanik der Elektronen in Kristallgittern". In: *Zeitschrift für Physik* 52.7 (July 1929), pp. 555–600. ISSN: 0044-3328. DOI: 10.1007/BF01339455. URL: https://doi.org/10.1007/BF01339455.

[36] Tianyu Zhu and Troy Van Voorhis. "Understanding the Dipole Moment of Liquid Water from a Self-Attractive Hartree Decomposition". In: *The Journal of Physical Chemistry Letters* 12.1 (2021). PMID: 33296211, pp. 6–12. DOI: 10.1021/acs.jpclett.0c03300. eprint: https://doi.org/10.1021/acs.jpclett.0c03300. URL: https://doi.org/10.1021/acs.jpclett.0c03300.

[37] Graeme Henkelman, Blas P. Uberuaga, and Hannes Jónsson. "A climbing image nudged elastic band method for finding saddle points and minimum energy paths". In: *The Journal of Chemical Physics* 113.22 (Dec. 2000), pp. 9901–9904. ISSN: 0021-9606. DOI: 10.1063/1.1329672. eprint: https://pubs.aip.org/aip/jcp/article-pdf/113/22/9901/10828159/9901_1_online.pdf. URL: https://doi.org/10.1063/1.1329672.

[38] Anton Kokalj. "Computer graphics and graphical user interfaces as tools in simulations of matter at the atomic scale". In: *Computational Materials Science* 28.2 (2003). Proceedings of the Symposium on Software Development for Process and Materials Design, pp. 155–168. ISSN: 0927-0256. DOI: https://doi.org/10.1016/S0927-0256(03)00104-6. URL: https://www.sciencedirect.com/science/article/pii/S0927025603001046.

[39] L. Pauling. *The Nature of the Chemical Bond and the Structure of Molecules and Crystals: An Introduction to Modern Structural Chemistry*. George Fisher Baker Non-Resident Lecture Series. Cornell University Press, 1960. ISBN: 9780801403330. URL: https://books.google.it/books?id=L-1K9HmKmUUC.